Analysis and discussion of two fluid modelling of pipe flow of fully suspended slurry

Gianandrea Vittorio Messa, Václav Matoušek

PII: S0032-5910(19)30742-9

DOI: https://doi.org/10.1016/j.powtec.2019.09.017

Reference: PTEC 14691

To appear in: *Powder Technology*

Received date: 20 December 2018

Revised date: 13 May 2019

Accepted date: 7 September 2019

Please cite this article as: G.V. Messa and V. Matoušek, Analysis and discussion of two fluid modelling of pipe flow of fully suspended slurry, *Powder Technology*(2018), https://doi.org/10.1016/j.powtec.2019.09.017

Analysis and Discussion of Two Fluid Modelling of Pipe Flow of Fully Suspended Slurry

Gianandrea Vittorio Messa[a,*], Václav Matoušek[1],

[a]*DICA, Politecnico di Milano, Piazza Leonardo da Vinci, 32, 20133 Milano, Italy*

[b]*The Czech Academy of Sciences, Institute of Hydrodynamics, Pod Pat'ankou 30/5, Prague 166 12, Czech Republic*

Abstract

Thanks to the advancements in computer power and capability of Computational Fluid Dynamics codes, the amount of research work on the numerical simulation of slurry flows in pipelines has increased exponentially in few years, opening the way to the use of this approach for engineering purposes. The Two Fluid Model (TFM), in which both phases are interpreted as interpenetrating continua and solved in the Eulerian, cell-based framework, allows the best compromise considering the engineering requirements of computational efficiency, applicability, and accuracy. However, the solution of this model is affected by several numerical and modelling factors, and, even if good agreement is achieved between simulation results and experimental measurements, it might be difficult to trust the predictions outside the validation conditions, thereby limiting the engineering potential of the two-fluid approach. The fully-suspended slurry flow in horizontal pipes was numerically simulated using the TFM recently developed by one of the authors of this paper, and the computational results were compared to experimental data reported in the literature. It has been clearly demonstrated that, even in this simple geometry, many possible sources of inaccuracy and uncertainty come into play. Whilst assessing their role, best practice guidelines and consistency checks were proposed to improve the accuracy of the estimates and increase the reliability of the TFM solution. Afterwards, pipe size-up scaling tests and a careful specification of the applicability conditions provided further confidence to the use of the TFM as a tool for

* Corresponding author

Email addresses: gianandreavittorio.messa@polimi.it (Gianandrea Vittorio Messa), matousek@ih.cas.cz (Václav Matoušek)

engineering design.

Keywords: hydraulic conveying, slurry flows, Two Fluid Model, sensitivity analysis, validation

Nomenclature

ΔA	area of influence of the data point in Fig. 4a (L^2)
$C_{1\varepsilon}$	constant in Eq. 12 (-)
$C_{2\varepsilon}$	constant in Eq. 12 (-)
C_μ	constant in Eq. 13 (-)
C_d	drag coefficient (-)
D	pipe diameter (L)
$\mathcal{D}$	phase diffusion term ($ML^{-3}T^{-1}$ [ϕ])
d_p	equivalent particle diameter (L)
d_p^+	dimensionless particle size (-)
$d_\mathrm{p}^{+\mathrm{B}}$	estimate of d_p^+ using Eq. 42 (-)
E	roughness parameter (-)
F_L	coefficient in Eq. 43 (-)
I	turbulence intensity of the liquid phase (-)
i_m	hydraulic gradient (-)
k	turbulent kinetic energy of the liquid phase (L^2T^{-2})
$\dot{M}$	mass flux ($ML^{-2}T^{-1}$)
N	number of spatial subdivisions (-)
$\tilde{N}$	number of interpolation points (-)
n	number of particle size classes (-)
n_p	particle number density (L^{-3})
P	locally-averaged pressure ($ML^{-1}T^{-2}$)
P_k	volumetric production rate of k (L^2T^{-3})
Re_m	modified particle Reynolds number, Eq. 10 (-)

Re^{w} wall Reynolds number (-)

r radial coordinate (L)

s friction factor (-)

U component of vector $\boldsymbol{U}$ (LT^{-1})

U^{*} friction velocity (LT^{-1})

V_{m} slurry bulk-mean velocity (LT^{-1})

V_{dl} deposition-limit velocity (LT^{-1})

w_{t} terminal settling velocity of a particle in quiescent liquid (LT^{-1})

x horizontal coordinate (L)

y vertical coordinate (L)

y^{+} dimensionless distance of the first grid point to the wall (L)

z axial coordinate (L)

Greek Symbols

α locally-averaged volume fraction (-)

β parameter of the two-fluid model (-)

γ horizontal chord in the pipe section

Δ parameter in Eq. 44 (-)

δ normal distance of the first grid point to the wall (L)

ε turbulence dissipation rate of the liquid phase ($L^{2}T^{-3}$)

θ azimuthal coordinate (-)

κ von Karman constant (-)

μ dynamic viscosity ($ML^{-1}T^{-1}$)

μ_{m} friction, mixture-viscosity related parameter ($ML^{-1}T^{-1}$)

μ_{t} eddy viscosity ($ML^{-1}T^{-1}$)

Π circumference in the pipe section, Fig. 15

ρ density (ML^{-3})

σ turbulent Schmidt number for volume fractions (-)

σ_{k} constant in Eq. 11 (-)

σ_ε constant in Eq. 12 (-)

τ shear stress ($ML^{-1}T^{-2}$)

ϕ generic transported variable

φ average angle of concentration profile, Fig. 12 (°)

Vectors

$\mathbf{F}_d$ drag force (MLT^{-2})

$\mathbf{g}$ gravitational acceleration vector (LT^{-2})

$\boldsymbol{M}$ interfacial momentum transfer term ($ML^{-2}T^{-2}$)

$\boldsymbol{n}$ unit normal vector (-)

$\boldsymbol{U}$ locally-averaged velocity vector (LT^{-1})

$\boldsymbol{U}^A$ projection $\boldsymbol{U}$ on the pipe section plane (LT^{-1})

$\boldsymbol{U}^{//}$ component of $\boldsymbol{U}$ parallel to the wall at the near-wall nodes (LT^{-1})

$\boldsymbol{W}$ locally-averaged slip velocity vector (LT^{-1})

Subscripts and superscripts

1,2 index of cells for i_m^{num} calculation

axis at pipe axis

exp experimentally-determined

k phase indicator

i index of horizontal position in Fig. 4b

In at the inlet boundary

j index of vertical position in Figs. 4a and 4b

l liquid phase

lam laminar

m mixture

num numerically-determined

out at the outlet boundary

p physical particle

ref reference factor for normalization

s	solid phase
turb	turbulent
w	at the wall / in the near-wall cells
θ, r, z	along direction θ, r, z

Operators

+	transpose
$\langle ... \rangle_A$	average over pipe area
$\langle ... \rangle_\Gamma$	average over near-wall cells
$\langle ... \rangle_\gamma$	average over horizontal chord
$\langle ... \rangle_\Pi$	average over circumference Π
$\sim$	interpolation from nearest nodes
$-$	arithmetic mean

Acronyms

BF	Bed Flow
CFD	Computational Fluid Dynamics
DPM	Discrete Particle Method
FS	Fully Suspended flow
HS	Heterogeneous Suspension
IPS	AInter-Phase Slip Algorithm
KTGF	Kinetic Theory of Granular Flow
LES	Large Eddy Simulation
MAE	Mean Absolute Error
MAPE	Mean Absolute Percentage Error
MB	Moving Bed flow
MFM	Multi Fluid Model
MM	Mixture Model
PS	Pseudo-homogeneous Suspension
RANS	Reynolds-Averaged Navier-Stokes

SB Stationary Bed flow

TFM Two Fluid Model

1. Introduction

The transport of liquid-solid slurries in pipes is encountered in various industrial processes such as mining, oil extraction, power generation, chemical production, and so on. Disposing of methods for estimating the behavior of the flowing slurries is fundamental for the proper design and management of the pipeline system.

Obviously, when developing predictive models, the fundamental physical features of slurry pipe flows must be taken into account. Of particular importance is the form in which the solids are conveyed, often referred to as flow regime. In horizontal pipe flows, a well established classification is that proposed by Doron and Barnea [1], who identified three different main patters in relation to slurry velocity and particle size. If relatively small solids are transported at high velocity, the turbulence of the fluid is enough to keep all the solids suspended, and Fully Suspended (FS) flow is likely to occur. This regime can be further divided into homogeneous suspension and Pseudo-homogeneous Suspension (PS), in which the distribution of the solid over the pipe section is nearly uniform, and Heterogeneous Suspension (HS), in which there is a concentration gradient along the vertical direction. As the slurry velocity decreases or the particle size increases, a transition is possible to the following regimes, namely: (a) flow with a Moving Bed (MB), in which the particles accumulate at the bottom of the pipe and form a packed bed sliding along the flow path. On top of this bed, HS is observed; (b) flow with a Stationary Bed (SB), in which stationary deposits are formed at the pipe invert whereas, in the rest of the pipe, the particles are transported as a separate moving layer and heterogeneous mixture. In addition to the above discussion, it is worth mentioning that slurry flows with very high solid concentration (say, exceeding of about 0.40 by volume) cannot be regarded as fully suspended even at high velocity. The reason is that the particles tend to develop mutual contacts (and contacts with the pipe wall), which significantly increase flow friction [2]. Such flows are primarily governed by interparticle collisions and the turbulence of the carrier fluid does not play a major role in suspending the solids. This situation will be further considered in Section 3.7.

The engineering assessment of slurry pipelines requires estimating macroscopic variables such as the hydraulic gradient, i_m (i.e. the frictional loss in height of water per unit length), the

deposition-limit velocity, V_{dl} (i.e. the slurry velocity below which solid deposit is observed), or the height of the stationary/moving bed in a stratified flow. Traditionally, simplified models calibrated with laboratory experiments have been regarded as an effective way to gather the essential information for the design and verification of slurry pipes without excessive mathematical complexity. For instance, the equivalent-fluid model, in which the slurry is interpreted a single-phase fluid with adjusted physical and rehological properties [3], has been an attempt to describe the hydraulic gradient of non-settling slurries in which viscous effects and non-Newtonian behavior are both important. At the opposite extreme, layered models are available for application fully or partially stratified flows of settling slurries [4–6]. As far as the estimation of the V_{dl} is concerned, several analytical or graphical methods have been reported in the literature, e.g., [7–10]. A correlation recently developed by Thomas [11] covers the flow conditions condidered in this study, and it will be subject of discussion in Section 3.7.

The rapidly increasing computer power allowed for a widespread diffusion of commercial and open source codes capable of modeling complex physics in realistic geometries. This opened the way to the possibility of improving the engineering handling of slurry flows by complementing the traditional approaches with the numerical simulation. For instance, as remarked by Uzi and Levy [12], Computational Fluid Dynamics (CFD) allows investigating specific phenomena occurring at the grain scale, such as pipeline erosion or particle degradation, which cannot be addressed by a simplified, global-scale model. Moreover, the detailed information provided by CFD simulations might be useful to find the origin of experimental observations which are still unexplained, such as the altered frictional head loss in bimodal slurry flows [13]. In addition, the numerical approach has the potential to overcome the size limitations associated with laboratory constraints, which make experimental data for pipe diameters larger than about 150 mm extremely rare. Finally, it opens the way to the prediction of slurry flows in more complex geometries than straight pipes (e.g. pipe bends, connections, valves) which are even harder to test experimentally.

Fig. 1. Classification of the CFD models for the simulations of slurry flows.

Generally, the CFD approaches for the simulation of slurry flows can be classified into different categories (Fig. 1). In the Eulerian-Lagrangian approach [14], the liquid phase is modeled as a continuum and solved in an Eulerian, cell-based framework, whereas the behavior of the solid

phase is obtained by the Discrete Particle Method (DPM), in which the individual trajectories of computational particles are calculated in a Lagrangian fashion. The coupling regime between the two phases depends on the amount of solids in the flow, and it ranges from one-way coupling for dilute slurries (i.e. the particles do not affect the liquid flow field) to four-way coupling for dense slurries (where the particle-particle and particle-fluid interactions are important). In the Eulerian-Eulerian approach [14], often referred to as Two Fluid Model (TFM), both phases are modeled as interpenetrating continua, and two sets of conservations equations are solved coupled in the Eulerian framework. Four-way coupling effects are indirectly accounted for by constitutive equations for the solid phase. The Mixture Model (MM) [15], sometimes referred to as Drift-Flux Model [16], might be interpreted as a simplified formulation of the two-fluid approach, which is valid under the hypothesis that the particles are rapidly accelerated to their terminal velocity. This assumption is called "local equilibrium approximation" and, broadly speaking, is acceptable if the particles are sufficiently fine. The MM solves for the fundamental conservation equations of the solid-liquid mixture and the mass conservation equation for the solid phase, all in the Eulerian form. In addition to the constitutive equations for the mixture, an algebraic, linearized equation for the slip velocity, i.e. the relative velocity between the two phases, is required to close the system of equations. For the sake of completeness, it is mentioned that, if the particles are particularly fine, the flow of a liquid-solid slurry might also by modeled by solving the conservation equations for a single-phase fluid with appropriate rheology. This can be regarded as a local generalization of the equivalent liquid model previously discussed, and, owing to the limited applicability, it will not be considered further in this research work. As highlighted in Fig. 1, the approaches listed in the same order as above are characterized by reduced level of physical insight and, at the same time, increased restrictiveness of the assumptions underlying their derivation and/or number of uncertain submodels and calibration parameters. This is also accompanied by substantial variation in computational burden, which, given the time requirements imposed by the engineering tasks, is a fundamental feature to take into account when assessing of the practical impact of a CFD model.

Table 1

Previous numerical studies on slurry pipe flows.

Reference	Approach	Flow regi	Flui d	Particles	ρ_p [kg/	d_p [mm]	D [mm]	V_m [m/s]	$\langle \alpha_s \rangle_A$ [-]

		me			m^3]				
Capecelatro and Desjardins [17]	LES+DPM	SB, HS	water	sand	2650	0.165	51.5	0.83, 1.6	0.084
Arolla and Desjardins [18]a	LES+DPM	SB, HS	water	sand	2650	0.280	69	-	-
Uzi and Levy [12]	RANS+DPM	MB, HS	brine	NaCl	2150	1.0-4.0	50-100	0.6-4.0	0.05-0.30
Hernández et al. [21]	(KTGF)-TFM	HS, PS	water	sand	≈ 2381	0.030-0.110	22.1	1.0-3.0	0.0025-0.20
Bossio et al. [22]	(KTGF)-TFM	MB, HS, PS	laterite	sand	2381	0.110	26.84	0.671-4.697	0.036-0.083
Ekambara et al. [23]	KTGF-TFM	BF, FS	water	sand, glass beads	2470, 2650	0.090-0.500	50-500	1.5-5.5	0.08-0.45
Antaya et al. [24]	KTGF-TFM(MFM)	FS	water	sand	2650	0.100-0.370	51.5, 150	2.0-6.0	0.20-0.43
Hashemi et al.[25]	KTGF-TFM	-	water	sand	2650	0.370	265	4.0, 6.0	0.20-0.40
Kaushal et al. [26]	KTGF-TFM, MM	FS	water	glass beads	2470	0.125	54.9	1.0-5.0	0.30-0.50
Gopaliya and Kaushal [27]	KTGF-TFM	FS	water	sand	2650	0.18-2.4	53.2	1.8, 3.1	0.15-0.45
Gopaliya and Kaushal	KTGF-TFM	FS	water	sand	2650	0.165-0.55	263	3.5-4.7	0.10-0.34

[28]									
Kumar et al. [29]	KTGF-TFM	FS	water	iron ore	4350	0.012	105	1.35-5.11	0.0263-0.31
Singh et al. [30]	KTGF-TFM	FS	water	coal	1560	0.059-0.206	50-150	2-5	0.30-0.60
Roco and Balakrishnam [33]	TFM	BF, FS	water	sand, glass beads	-	0.165-0.580	40, 51.5	1.05-4.17	0.07-0.189
Messa et al. [35]	TFM	FS	water	sand, glass beads	2440, 2650	0.090-0.370	53-150	1.33-8.0	0.11-0.40
Messa et al. [36]	TFM	FS	water	sand, glass beads	2440, 2650	0.090-0.520	50.7-150	1.33-8.0	0.09-0.40
Messa and Malavasi [37]	TFM	MB, FS	water	sand	≈ 2650	0.090-0.520	50.7-150	1.33-6.0	0.09-0.43
Messa and Malavasi [38]	TFM	FS	water	sand	≈ 2650	0.090-0.640	50-200	2.0-9.0	0.07-0.41
Chen et al. [39]	KTGF-MFM	HS, PS	water	coal	1465	0.065+0.345	25-50	0.2-5	0.38-0.538
Li et al. [40]	KTGF-MFM	MB, HS, PS	water	glass beads	2470	0.125+0.440	54.9	2.0-5.0	0.20-0.50
Li et al. [41]	KTGF-MFM	MB, HS, PS	water	glass beads	2470	0.125+0.440	54.9	2.0-4.0	0.20-0.40
Ling et al. [42]	MM	BF, FS	water	silica/zircon sand	2380, 4223	0.11	22.1	1.0-3.0	0.10, 0.20
Lin and	MM	BF,	wate	silica/zir	2380,	0.11	22.1	1.0-3.0	0.10,

Ebadian [43]		FS	r	con sand	4223				0.20
Silva et al. [44]	MM	SB, MB, FS	salin e wate r	glass beads	2500	0.10-0.6 0	100	1.0-3.0	0.008-0. 11

[a] Instead of making reference to V_m and C_{vi}, the authors provided the superficial velocity of the liquid (0.3, 0.4, and 0.6 m/s) and the mass flow rate of the injected particles (2.2 g/s).

A summary of the most relevant numerical studies on slurry flows in horizontal pipes published so far is reported in Table 1, alongside with the adopted modelling approach and the key physical parameters, namely the flow regime, the type of carrier fluid, the particle material, the particle density, ρ_p, the characteristic particle size, d_p, the pipe diameter, D, the bulk-mean velocity of the mixture, V_m, and the area-averaged solid volumetric concentration, $\langle \alpha_s \rangle$. The characteristic size of non spherical solids can be taken as the equivalent particle diameter, i.e. the diameter of a sphere having the same volume of the actual particle. Note that, the flow regime indicated in the table was that declared in the published articles, and was not inferred by the authors from inspection of the experimental data. In the lack of specific information, general categories like Fully Suspended (FS, which can be either PS or HS) or Bed Flow (BF, which indicates either SB or MB) were considered.

To the authors' best knowledge, the Eulerian-Lagrangian approach was employed for this kind of application only by Capecelatro and Desjardins [17], Arolla and Desjardins [18], and Uzi and Levy [12]. Particularly, Capecelatro and Desjardins [17] used the Large Eddy Simulation (LES) method [19] to simulate the turbulent flow of the liquid phase, coupling the fluid flow equations with the DPM. Two scenarios were analyzed with the high level of detail allowed by the modelling approach used in the study. The flow regime was either SB or HS and, besides exploring macroscopic parameters such as mean volume fraction distribution, the mean fluid velocity profile, and the hydraulic gradient, the authors mainly focused on the statistical description of the particle motion in the turbulent flow. A couple of years later, Arolla and Desjardins [18] used the same numerical setup to characterize the two-phase flow field and the flow pattern for increasing values of liquid superficial velocity, which resulted in a transition from SB to HS. The authors

analyzed first-order statistics, but mostly focused on the topological structure of the solid-liquid interface. In the Eulerian-Lagrangian model employed by Uzi and Levy [12], the turbulence in the liquid phase is handled by a computationally cheaper Reynolds-Average Navier-Stokes (RANS) technique. The authors investigated the pipe transportation of coarse NaCl particles in brine in both the HS and MB flow regimes, and carried out an extensive analysis of the influence of the problem governing parameters (i.e. conveying velocity, particle concentration, particle size, and pipe diameter) on the characteristics of the two-phase flow.

However, the majority of the earlier CFD investigations of slurry pipe flows were performed using the Two Fluid Model, which provides a good compromise between accuracy and computational cost. The TFM provide only a locally averaged picture of the turbulent slurry flow, which is derived from different averaging procedures, as discussed by Burns et al. [20]. In most TFMs, constitutive equations for the solid phase derived from the Kinetic Theory of Granular Flow (KTGF) were employed. The studies by Hernández et al. [21] and Bossio et al. [22], developed with the Ansys CFX commercial code, relied on some KTGF-based closures to briefly explore the behavior of slurry with Newtonian (water) and non-Newtonian (laterite) carrier fluid. Using the same software, Ekambara et al. [23] performed an extensive validation study based on experimental data taken from the literature. The authors assessed the predictive capacity of the computational model for different flow conditions, mostly in terms of concentration profiles, but they also explored the hydraulic gradient and the velocity profile. Subsequent studies from the same research group [24, 25] reported the analysis of the influence of some features of the TFM (e.g., turbulence model, wall boundary conditions, and interstitial forces) and its validation with respect to concentration and velocity measurements. Kaushal et al. [26] made use of the granular model embedded in the Ansys Fluent code to simulate the slurry flow of fine glass beads at high concentration in the FS regime. The authors analyzed the structure of the two-phase flow for different combinations of slurry velocity and concentration, and reported fairly good agreement with the experimental evidence for hydraulic gradient and solids concentration profile. The same TFM, with slight variations in the closures, was employed to investigate the behavior of sand-water, iron ore water, and coal-water mixtures with different flow characteristics in subsequent works [27–30]. Finally, it is noted that the modeling considerations drawn in the above mentioned studies apply also when KTGF-TFMs are employed to simulate completely different types of slurries, such as the slush nitrogen cryiogenic fluids investigated by Jiang and Zhang [31,

32].

In addition to the pioneering work by Roco and Balakrishnam [33] and the brief exploration by Chen [34], the research works authored by Messa et al. [35–38] are one of the few attemps of reproducing the behavior of pipe slurry flows using TFMs not based on the KTGF. The TFM developed by Messa and co-workers, implemented in the PHOENICS commercial code, relies on (semi) empirical constitutive equations for the solid phase and on a peculiar treatment of particle turbulent dispersion and inter-phase momentum exchange. Based on an extensive comparison against laboratory experiments, the model proved capable of producing accurate estimation of the hydraulic gradient, the concentration profile, and the mixture velocity profile provided that the flow is fully-suspended. Furthermore, the mathematical structure of the model's equations and the solution algorithms embedded in the PHOENICS code contributed to its high numerical performance.

It is well known that one of the main limitations of the TFM is due to the fact that solid phase is described by a single representative particle size, implicitly assuming the particles to be monodisperse. The simulation of polydisperse slurries by means of the Eulerian approach requires a generalization of the TFM, in which the particle size distribution is divided into n classes, each characterized by a representative sizes, and n sets of mass and momentum conservation equations are solved coupled together will all closures. Such Multi Fluid Model (MFM) extends the capability of the TFM, but, at the same time, it increases the number of submodels and parameters and entails a number of numerical complications. Probably also because of these reasons, the application of the MFM to the simulation of slurry pipe flows is still in the exploratory stage, and, to the authors' best knowledge, limited to bimodal mixtures with two characteristic particle sizes (n=3). Chen et al. [39] used such a kind of model to investigate the fluid-dynamic behavior of coal-water slurries, reporting fairly good agreement with concentration profile and hydraulic gradient measurements. Li et al. [40, 41] focused on glass bead slurries and, after successfully validating their CFD model against data from the literature, they extensively analyzed the structure of the flow, paying particular attention on the differences between single- and multi-sized mixtures. Finally, it is noted that, in their already mentioned paper, Antaya et al. [24] explored the use of a MFM to simulate a bimodal mixture, but they ignored the influence of particle-particle interactions between the dispersed phases.

Conversely, a computationally efficient simulation of an arbitrary number of particle

fractions is possible with the Mixture Model, but the strong assumptions underlying this modelling approach reduces its applicability to a restricted class of slurry flows. In their pioneering works, Ling et al. [42] and Lin and Ebadian [43] noted that the MM allowed accurate hydraulic gradient predictions above the limit-deposit velocity. Some years later, based on a more extensive experimental validation, Kaushal et al. [26] found that, for fully-suspended slurry flow of small particles (≈ 0.125 mm) at high concentration (0.30-0.50) and velocity, the MM strongly overestimates the hydraulic gradient, and it is less accurate than the TFM in estimating the concentration profile. Recently, Silva et al. [44] reported that, provided that its closures are properly set, the MM might allow reliable description of glass bead slurry flows at high velocity and low concentration (¡0.11), even in the presence of coarse particles with ≈ 0.5 mm size. For the sake of completeness, it is noted that the MM has been applied to horizontal slurry pipe flows with different characteristics than those of interest in this study, such as ice slurries [45] or mixtures of neutrally-buoyant polystyrene particles in water [46].

The literature survey reported above highlights that the number of scientific articles on the CFD simulation of slurry pipe flows has increased exponentially in recent years. With a some valuable exceptions, many of these studies follow a similar methodological approach, namely experimental verification of the CFD model for a specific set of flow conditions and use of the validated model to infer non measurable features of the flow. Such approach is certainly suitable to gain further insight into the behavior of a particular slurry flow, but it does not allow for the assessment of the predictive capacity of the model outside the verification range, limiting its usefulness for engineering design of, for instance, large size pipes or complex pipeline equipment. Believing that the achievement of this objective will have positive impact on the engineering use of CFD for industrial slurry flow modelling, a critical analysis is presented for the benchmark case of straight horizontal pipe, with the goal of highlighting the modeling features most worthy of attention and providing best practice guidelines for future studies and application. The issues of numerical convergence, physical consistency, sensitivity upon the model's parameters, and calibration of the tuning constants will be discussed in detail before turning the attention on two aspects of particular engineering relevance, namely, the pipe size-up scalability and the specification of the applicability conditions.

Consistently with the application-oriented view of this study, the attention was focused on the TFM, which, being computationally cheaper than the DPM and not relying on the restrictive

assumptions of the MM, seems the most practical for engineering purposes. Furthermore, the TFM depends on several submodels and parameters that might act as sources of uncertainty on the numerical estimates, and, therefore, their roles require to be established. Particularly, the TFM developed by Messa and co-workers in the formulation reported in [38] was considered in this investigation, and given a deeper physical interpretation; however, a lot of effort was devoted to providing recommendations of general validity. From this perspective, all numerical results were discussed and compared with those of the earlier investigations summarized in Table 1.

2. Mathematical modelling

In this section, the equations of the TFM will be provided alongside with the relevant details regarding the numerical setup.

2.1. The β-σ Two Fluid Model

As already mentioned, in the TFM the flow of the ensemble of particles, referred to as "solid phase", is modeled in the Eulerian frame of reference and solved coupled with that of the carrier fluid phase. Hereafter, the subscripts "p", "l", and "s" will be used to denote the physical particles, the liquid phase, and the solid phase, respectively. In this study, the flows were simulated as statistically steady, thereby dropping the time derivative terms. Therefore, the phasic continuity and momentum equations, obtained from the formulation of the model reported in Messa and Malavasi [38], read as follows

$$\nabla\left(\alpha_{\mathrm{l}}\rho_{\mathrm{l}}\boldsymbol{U}_{\mathrm{l}}\right)-\nabla\cdot\left(\frac{\mu_{\mathrm{t,l}}}{\sigma}\nabla\alpha_{\mathrm{l}}\right)=0 \tag{1}$$

$$\nabla\left(\alpha_{\mathrm{s}}\rho_{\mathrm{s}}\boldsymbol{U}_{\mathrm{s}}\right)-\nabla\cdot\left(\frac{\mu_{\mathrm{t,l}}}{\sigma}\nabla\alpha_{\mathrm{s}}\right)=0 \tag{2}$$

$$\begin{aligned}\nabla\left(\alpha_{\mathrm{l}}\rho_{\mathrm{l}}\boldsymbol{U}_{\mathrm{l}}\boldsymbol{U}_{\mathrm{l}}\right)=&-\alpha_{l}\nabla P+\nabla\cdot\left[\alpha_{\mathrm{l}}\left(\mu_{\mathrm{l}}+\mu_{\mathrm{t,l}}\right)\nabla\boldsymbol{U}_{\mathrm{l}}\right]+\\&+\alpha_{l}\rho_{l}\boldsymbol{g}+\boldsymbol{M}_{l}+\nabla\cdot\left(\frac{\mu_{\mathrm{t,l}}}{\sigma}\boldsymbol{U}_{\mathrm{l}}\nabla\alpha_{\mathrm{l}}\right)\end{aligned} \tag{3}$$

$$\nabla\left(\alpha_{\mathrm{s}}\rho_{\mathrm{s}}\boldsymbol{U}_{\mathrm{s}}\boldsymbol{U}_{\mathrm{s}}\right)=-\alpha_{s}\nabla P+\nabla\cdot\left[\alpha_{\mathrm{s}}\left(\mu_{\mathrm{s}}+\mu_{\mathrm{t,s}}\right)\nabla\boldsymbol{U}_{\mathrm{s}}\right]+ \\ +\alpha_{s}\rho_{s}\boldsymbol{g}+\boldsymbol{M}_{s}+\nabla\cdot\left(\frac{\mu_{\mathrm{t,l}}}{\sigma}\boldsymbol{U}_{\mathrm{s}}\nabla\alpha_{\mathrm{s}}\right) \tag{4}$$

In the equations above, α is the locally-averaged volume fraction, whose physical characterization is still subject of discussion for TFMs applied to turbulent flows. Following Burns et al. [20], in the current TFM formulation α can be interpreted as the time-average value of the proportion of local volumetric space occupied by a phase. Other symbols are as follow, namely, ρ is the density, $\boldsymbol{U}$ is the locally-averaged velocity vector, σ is the turbulent Schmidt number for volume fraction, P is the locally-averaged pressure, μ and μ_{t} are the dynamic viscosity and the eddy viscosity, respectively, $\boldsymbol{g}$ is the gravitational acceleration vector, and $\boldsymbol{M}$ is the interfacial momentum transfer term, which will be discussed later. Note that, owing to the global continuity equation, the two volume fractions α_{l} and α_{s} must sum to unity.

One of the key features of the two-fluid model, inherited from the original Inter-Phase Slip Algorithm (IPSA) of Spalding [47], resides in the presence, in all conservation equations, of diffusive terms having the following form

$$\mathcal{D}_{k}=\nabla\cdot\left(\frac{\mu_{\mathrm{t,l}}}{\sigma}\phi_{k}\nabla\alpha_{k}\right) \tag{5}$$

where k is a phase indicator parameter, being equal to either l or s, and ϕ has unit value in the mass conservation equations, whereas it stands for the generic transported variable in all other equations. As it has been well documented in Burns et al. [20], these terms, referred to as "phase diffusion fluxes", arise from the modelling of the correlations between the fluctuating velocity and the fluctuation volume fractions.

Another peculiarity of the current TFM is the introduction of an empirical parameter, μ_{m}, related to the interactions among the particles in the slurry. The variable μ_{m} is a function of the local solid volume fraction, and it is calculated as

$$\mu_{\mathrm{m}}=\mu_{\mathrm{l}}\left\{\frac{2.5}{\beta}\left\lfloor\frac{1}{\left(1-\alpha_{\mathrm{s}}\right)^{\beta}}-1\right\rfloor\right\} \tag{6}$$

where β is a tuning factor, which governs how quickly μ_{m} increases with α_{s} and, in [38], it was associated with the physical characteristics of the solid grains (i.e. material and shape). Given

the formal equality between Eq. 6 and the comprehensive formula for the viscosity of a mixture proposed by Cheng and Law [48], μ_m might be referred to as "friction, mixture-viscosity related parameter". However, note that this parameter has a completely different meaning here.

The quantity μ_m appears in the evaluation of the viscosity of the solid phase, μ_s, which is obtained by assuming the following relationship:

$$\mu_m = \alpha_l \mu_l + \alpha_s \mu_s \tag{7}$$

It also comes up in the calculation of the interfacial momentum transfer term, $\boldsymbol{M}$. This vector, having the dimension of a force per unit volume, represents the local average transfer of momentum between the phases, which, after preliminary sensitivity analyses, was attributed uniquely to the effect of the drag. Thus, the expression of $\boldsymbol{M}$ was

$$\boldsymbol{M}_l = -\boldsymbol{M}_s = n_p \boldsymbol{F}_d = \frac{\alpha_s}{\frac{4}{3}\pi\left(\frac{d_p}{2}\right)^3} \cdot \frac{1}{2}\rho_l \left(\pi \frac{d_p^2}{4}\right) C_d \,|\boldsymbol{W}|\boldsymbol{W} \tag{8}$$

where n_p is the particle number density, that is, the number of particles per unit volume of slurry, $\boldsymbol{F}_d$ is the drag force, calculated with respect to the local mean velocities, C_d is the drag coefficient, and $\boldsymbol{W}$ is the mean slip velocity vector, i.e. the difference between $\boldsymbol{U}_l$ and $\boldsymbol{U}_s$. The term C_d, in turn, was obtained by the following formula, analog of the Schiller and Naumann correlation for the drag coefficient on a single sphere [49]:

$$C_d = \max\left[\frac{24}{Re_m}\left(1 + 0.15 Re_m^{0.687}\right), 0.44\right] \tag{9}$$

in which Re_m was defined as

$$Re_m = \frac{\rho_l d_p \,|\boldsymbol{W}|}{\mu_m} \tag{10}$$

The evaluation of C_d in terms of Re_m instead of the more classical particle Reynolds number, based on the fluid viscosity, is a distinctive feature of the current TFM. This was an idea heuristically introduced by one of the authors of this paper in his PhD thesis [35] based on an analogy with the mixture-viscosity based approach implemented by Ishii and Mishima [51] in a TFM formulation. Due to the increase of μ_m with α_s, referring to Re_m allows correctly capturing the strong interactions between the phases which characterize dense slurry flows,

avoiding unphysically high solid volume fractions close to the pipe bottom. However, the analogy is purely formal since, as already remarked, μ_m is a friction parameter and not the viscosity of the mixture. Furthermore, the Re_m concept allows resolving any apparent inconsistency in the application of Eq. 9 to natural sands with non-spherical grain shape. The most commonly followed approach to account for the increased resistance experienced by non-spherical particles is to modify the drag coefficient via some particle shape related parameter, e.g. [52]. In the present TFM, the same effect is achieved through the empirical parameter β: compared to spherical particles, in fact, natural sands are associated higher β values. As a consequence, for a given solid volume fraction, such materials are characterized by higher μ_m and, in turn, lower Re_m and higher C_d.

The eddy viscosity of the liquid phase, $\mu_{t,l}$, was obtained from the two-phase extension of the k-ε standard turbulence model of Launder and Spalding for high Reynolds number flows [53], which is available as option in PHOENICS:

$$\nabla\left(\alpha_l\rho_l\boldsymbol{U}_l k\right)=\nabla\cdot\left[\alpha_l\left(\mu_l+\frac{\mu_{t,l}}{\sigma_k}\right)\nabla k\right]+ \\ +\alpha_l\rho_l\left(P_k-\varepsilon\right)+\nabla\cdot\left(\frac{\mu_{t,l}}{\sigma}k\nabla\alpha_l\right) \tag{11}$$

$$\nabla\left(\alpha_l\rho_l\boldsymbol{U}_l\varepsilon\right)=\nabla\cdot\left[\alpha_l\left(\mu_l+\frac{\mu_{t,l}}{\sigma_\varepsilon}\right)\nabla\varepsilon\right]+ \\ +\alpha_l\rho_l\frac{\varepsilon}{k}\left(C_{1\varepsilon}P_k-C_{2\varepsilon}\varepsilon\right)+\nabla\cdot\left(\frac{\mu_{t,l}}{\sigma}\varepsilon\nabla\alpha_l\right) \tag{12}$$

$$\mu_{t,l}=C_\mu\rho_l\frac{k^2}{\varepsilon} \tag{13}$$

where k and ε are the turbulent kinetic energy and the turbulent dissipation rate of the liquid phase, σ_k, σ_ε, $C_{1\varepsilon}$, $C_{2\varepsilon}$, and C_μ are dimensionless constants, and P_k is the volumetric production rate of k due to the working of the Reynolds stresses against the mean flow, calculated as

$$P_k=2\frac{\mu_l}{\rho_l}\cdot\frac{1}{2}\left[\nabla\boldsymbol{U}_l+\left(\nabla\boldsymbol{U}_l\right)^+\right]:\nabla\boldsymbol{U}_l \tag{14}$$

in which the subscript "+" indicates that the transport of the dyadic $\nabla \boldsymbol{U}_\mathrm{l}$ is taken. The values of the model constants were those indicated in Launder and Spalding [53], namely σ_k=1.0, σ_ε =1.314, $C_{1\varepsilon}$=1.44, $C_{2\varepsilon}$=1.92, and C_μ=0.09.

The evaluation of the eddy viscosity of the solid phase, $\mu_{\mathrm{t,s}}$, did not require solution of additional transport equations, since this parameter was directly obtained from $\mu_{\mathrm{t,l}}$, as follows

$$\mu_{\mathrm{t,s}} = \rho_\mathrm{s} \frac{\mu_{\mathrm{t,l}}}{\rho_\mathrm{l}} \tag{15}$$

As it will be discussed later in Section 3.4, the β factor in Eq. 6 and the turbulent Schmidt number in the phase diffusion fluxes, σ (Eq. 5), are the main calibration parameters of the TFM which, in order to highlight this aspect, was referred to as "β-σ model".

2.2. Computational domain and boundary conditions

The computational domain consists of a circular pipe of length equal to 120 pipe diameters, and the imposed boundary conditions are inlet, outlet, solid walls, and axis (Fig. 2). Indeed, the geometrical and flow symmetry of the problem could have been exploited by solving only over half of the pipe section, as in previous works [35, 36, 38]. Here, the choice of simulating the entire pipe section was intentional and served as further verification of the model's capability in reaching a converged, numerically stable, symmetrical solution.

Fig. 2. Computational domain and boundary conditions.

At the pipe inlet, the mass flow rates of the two phases, $\dot{M}_\mathrm{l}^\mathrm{in}$ and $\dot{M}_\mathrm{s}^\mathrm{in}$, the mean axial velocities of the two phases, $U_{\mathrm{l},z}^\mathrm{in}$ and $U_{\mathrm{s},z}^\mathrm{in}$, the turbulent kinetic energy of the liquid, k^in, and its dissipation rate, ε^in, were imposed. These variables were modelled as uniformly distributed over the inlet boundary, and calculated as:

$$U_{\mathrm{l},z}^\mathrm{in} = U_{\mathrm{s},z}^\mathrm{in} = V_\mathrm{m} \tag{16}$$

$$\dot{M}_\mathrm{l}^\mathrm{in} = \rho_\mathrm{l}\left(1-\langle\alpha_\mathrm{s}\rangle_A\right)V_\mathrm{m} \qquad \dot{M}_\mathrm{s}^\mathrm{in} = \rho_\mathrm{s}\langle\alpha_\mathrm{s}\rangle_A V_\mathrm{m} \tag{17}$$

$$k^{\text{in}} = \frac{3}{2}\left(I^{\text{in}} V_{\text{m}}\right)^2 \tag{18}$$

$$\varepsilon^{\text{in}} = C_{\mu}^{3/4} \frac{\left(k^{\text{in}}\right)^{3/2}}{0.07D} \tag{19}$$

where the area-averaged solid volume fraction, $\langle \alpha_{\text{s}} \rangle_A$, was obtained from the experimental measurements following the procedure presented in Section 3.1, and I^{in} is the turbulence intensity of the liquid, assumed equal to 0.05. As it is evident from the equations above, the two phases have been assumed to enter the domain with the same velocity and, therefore, no slip was allowed at the inlet section. As it will be thoroughly discussed in section 3.2, the length of the computational domain is sufficient to ensure that fully-developed flow conditions are achieved.

At the pipe outlet, the static gauge pressure is specified and held constant to a zero value, so that the volume fractions and mass outflows of the two phases result as part of the overall solution.

Fig 3. Sketch of a near-wall cell. Note that δ is the normal distance of the first grid point to the wall, whereas 2δ is the thickness of the near-wall layer of cells.

At the pipe wall, the equilibrium wall function of Launder and Spalding was employed to evaluate the wall shear stress of the liquid phase, $\tau_{\text{l}}^{\text{w}}$, and the values of the turbulent variables at the first-grid nodes, k^{w} and ε^{w} (Fig. 3). The following equations were solved

$$\tau_{\text{l}}^{\text{w}} = \rho_{\text{l}} s_{\text{l}} |\boldsymbol{U}_{\text{l}}^{//}|^2 \tag{20}$$

$$k^{\text{w}} = \frac{U_{\text{l}}^{*}}{\sqrt{C_{\mu}}} \tag{21}$$

$$\varepsilon^{\text{w}} = C_{\mu}^{3/4} \frac{\left(k^{\text{w}}\right)^{3/2}}{\kappa\delta} \tag{22}$$

where $\boldsymbol{U}_{\text{l}}^{//}$ is the resultant velocity of the liquid parallel to the wall at the first grid node, U_{l}^{*} is the friction velocity of the liquid, equal to $\sqrt{\tau_{\text{l}}^{\text{w}} / \rho_{\text{l}}}$, κ=0.41 is the von Karman constant, δ is the normal distance of the first grid point from the wall, and s_{l} is the friction factor of the liquid phase, calculated as

$$s_1 = \max\left(s_1^{\text{lam}}, s_1^{\text{turb}}\right) \tag{23}$$

with

$$s_1^{\text{lam}} = \frac{1}{Re_1^{\text{w}}} \qquad s_1^{\text{turb}} = \frac{\kappa^2}{\ln^2\left(E \cdot Re_1^{\text{w}} \sqrt{s_1^{\text{turb}}}\right)} \tag{24}$$

in which E is a roughness parameter, which was set as 8.6 as appropriate for smooth walls, and the wall Reynolds number Re_1^{w} is defined as

$$Re_1^{\text{w}} = \frac{\rho_1 |\boldsymbol{U}_1^{//}| \delta}{\mu_1} \tag{25}$$

The wall shear stress of the solid phase, $\tau_{\text{s}}^{\text{w}}$, was calculated as

$$\tau_{\text{s}}^{\text{w}} = \rho_{\text{s}} s_{\text{s}} |\boldsymbol{U}_{\text{s}}^{//}|^2 \tag{26}$$

where s_{s} and $\boldsymbol{U}_{\text{s}}^{//}$ are the analog of s_1 and $\boldsymbol{U}_1^{//}$ for the solid phase, respectively, and s_{s} is given by

$$s_{\text{s}} = \frac{\kappa^2}{\ln^2\left(E \cdot Re_{\text{s}}^{\text{w}} \sqrt{s_{\text{s}}}\right)} \tag{27}$$

where

$$Re_{\text{s}}^{\text{w}} = \frac{\rho_{\text{s}} |\boldsymbol{U}_{\text{s}}^{//}| \delta}{\mu_{\text{s}}} \tag{28}$$

The formulation of the wall boundary condition for the solid phase adopted in this study was proposed by Messa and Malavasi [38] based on an analogy with the equilibrium wall function of Launder and Spalding, and it requires the fulfillment of the constraint $d_{\text{p}}^{+} < 30$, where

$$d_{\text{p}}^{+} = \frac{\rho_1 d_{\text{p}} U_1^{*}}{\mu_1} \tag{29}$$

The use of a structured grid in cylindrical-polar coordinates, as detailed later, requires introducing a boundary condition at the pipe axis. The normal gradients for all dependent variables are zero there and, therefore, a zero-flux condition was applied along such boundary.

2.3. Solution strategy

The mathematical model described above was implemented in the CFD code PHOENICS version

2018 and solved numerically via the Finite Volume Method. This required integrating the built-in Eulerian, two-fluid, IPSA of Spalding [47] with user-defined functions and subroutines. The numerical settings were the same as in Messa et al. [36], namely: elliptic-staggered formulation, in which the scalar variables are evaluated at the cell centers and the velocity components at the cell faces; central differencing scheme and hybrid differencing scheme of Spalding [54] to discretize the diffusion and convection terms, respectively; SIMPLEST [55] and IPSA [47] algorithms of Spalding to iteratively solve the finite volume equations; slab-by-slab calculation procedure, in which all the dependent variables are solved at the current slab before the solver routine moves to the next slab; inertial relaxation applied to the momentum equations with a false-time step of 0.01 s, and linear relaxation factor of 0.4 applied to all other flow variables.

A structured mesh in cylindrical-polar coordinates was used to discretize the computational domain. The proper number and size of the subdivisions along the azimuthal, radial, and axial directions were established based on a grid independence study, which will be illustrated in section 3.3.

In PHOENICS, a global convergence condition was established as the sum of the absolute residual errors of all conservation equations being less than 0.01% of reference quantities based on the total inflow of the variable in question. In practice, a reasonably stable spread of the whole-field residuals was obtained after about 1000 iterations, and this was accepted as a criterion for stopping the solver. This required about half an hour CPU time using a computer with Intel Core i7-4790 CPU @ 3.60 GHz 3.60 GHz and 8.00 GB RAM.

3. Results and discussion

After presenting the experimental database considered for validating the β-σ model, and explaining the techniques for comparing experiments and simulation results (Section 3.1), important aspects of the Two-Fluid Modelling of fully-suspended flows will be investigated. Sections 3.2, 3.3 and 3.4 address the issues of domain definition, numerical convergence and tuning of the model's parameters, which are fundamental to guarantee the reliability of the TFM within the specific calibration range. Section 3.5 demonstrated that, within the calibration conditions, the β-σ model can be used for estimating difficult-to-measure yet engineering relevant quantities such as the wall shear stress or the velocity field. Finally, Sections 3.6 and 3.7

focus on two essential topics related with the β-σ model as a tool for engineering design, namely, the pipe size-up scalability and the specification of the applicability domain.

3.1. Experimental database for validation

Data collected in previous experimental campaigns, already reported in published literature [56–59] were selected for comparison with the numerical simulations, as summarized in Table 2. In particular, datasets A and B were collected by one of the authors of this paper in two different flow loops, located at the Institute of Hydrodynamics of the Czech Academy of Sciences in Prague and at the Delft University of Technology, respectively. Datasets C and D was obtained at Saskatchewan Research Council Pipe Flow Technology Centre by Randall Gillies and co-workers.

Table 2

Experimental datasets considered for comparison with the numerical simulations.

Dataset ID	Reference	Fluid	Particles	ρ_p [kg/m^3]	d_p [mm]	D [mm]	V_m [m/s]	$\langle\alpha_s\rangle_A$ [-]
A	Matoušek et al. [56]	water	glass beads	2450	0.180	100	1.48-4.0	0.10-0.36
B	Matoušek [57]	water	sand	2650	0.130	150	1.41-6.0	0.11-0.35
C	Gillies et al. [58]	water	sand	2650	0.090	102.7	1.33-3.0	0.19-0.33
D1	Gillies [59]	water	sand	2650	0.180	53.2	1.10-3.05	0.15, 0.30
D2	Gillies [59]	water	sand	2650	0.180	459	2.74-4.26	0.10-0.34

Considerable effort was devoted to the selection of the experimental data among those available in the literature. Finally, the datasets reported in Table 2 were judged suitable to provide a quantitative assessment of the models' capability, based on the following considerations. First, all the details needed to numerically reproduce the experiments were known and their output, i.e. hydraulic gradient and solids concentration profile, were available to the authors in tabular format.

Second, the number of simulated flow conditions was quite large, equal to 14, 12, 12, 22, and 43 for the five datasets. Third, although the database selection was limited by physical and numerical constraints (as detailed in Section 3.7), the datasets span over a rather wide range of slurry velocities, concentrations, and pipe diameter, and also the particle size changes. Particularly, dataset A allows testing the predictive capacity of the model in case of artificial solids, datasets B and C extend the validation to natural sands, and, finally, dataset D allows testing the model's capability to upscale to larger pipe diameters.

Fig. 4. Sketches showing (a) the local concentration data in the experiments and (b) the post-processing interpolation points in the numerical simulations.

In order to numerically reproduce the experiments, the pipe geometry, the characteristics of the solid particles, the slurry velocity, and the area-averaged volume fraction of the solid phase needed to be known. Generally, these quantities were directly provided by the experimenters. However, in datasets A to C, $\langle \alpha_s \rangle$ was estimated by post-processing the local concentration data. Particularly, in all laboratory campaigns use was made of radiometric devices which provide the chord-average volume fraction at different elevations above the pipe bottom (Fig. 4a). Starting from these measurements, the area-averaged volume fraction was calculated as:

$$\langle \alpha_s \rangle_A^{\exp} = \frac{\sum_j \langle \alpha_s \rangle_{\gamma_j}^{\exp} \Delta A_j}{\pi \frac{D^2}{4}} \tag{30}$$

where $\langle \alpha_s \rangle_{\gamma_j}^{\exp}$ is the experimentally determined chord-average volume fraction at location j and ΔA_j is the area of influence of the data point. The values of $\langle \alpha_s \rangle_A^{\exp}$ resulting from Eq. 30 were imposed at the inlet section in the CFD simulations (Eq. 17).

The comparison between the experiments and the computational simulations was made in terms of hydraulic gradient and concentration profile. The hydraulic gradient was numerically calculated as

$$i_m^{\text{num}} = \frac{1}{\rho_1 |\boldsymbol{g}|} \cdot \frac{P_1 - P_2}{z_2 - z_1} \tag{31}$$

where the subscripts 1 and 2 indicate two cells adjacent to the pipe axis and located in the region of

fully-developed flow, identified in the next section. For consistency with the measurement method, the concentration profile was defined as the chord-averaged one. That is, the y_j^{exp}-$\langle\alpha_\mathrm{s}\rangle_{\gamma_j}^{\mathrm{exp}}$ points were compared with the numerical analogue, obtained by interpolating the α_s field on a regular grid of points (i, j) and calculating $\langle\alpha_\mathrm{s}\rangle_{\gamma}^{\mathrm{num}}$ at elevation y_j^{num} as

$$\langle\alpha_\mathrm{s}\rangle_{\gamma_j}^{\mathrm{num}} = \frac{\sum_i \tilde{\alpha}_\mathrm{s}^{ij}}{\tilde{N}^j} \tag{32}$$

where $\tilde{\alpha}_\mathrm{s}^{ij}$ stands for the interpolated value of α_s at point (x_i, y_j), and $\tilde{N}^j$ is the number of interpolation points at elevation y_j. Figure 4b clarifies the followed procedure.

3.2. Identification of the region of fully-developed flow

Identifying the part of the domain in which the flow is fully developed, i.e. where $\partial/\partial z = 0$ for all fluid-dynamic variable except the pressure, is a fundamental step to validate the computational model, since the experimental data are usually collected in that region. This is strictly related with the type of imposed boundary conditions. Periodic boundary conditions produce fully-developed flow in the whole domain, and, therefore, a relatively short pipe length can be sufficient [12, 17, 18]. On the contrary, if inlet-outlet boundary conditions are employed, then the flow needs to develop from the distributions imposed at the entry section, thereby making it necessary to simulate a longer pipe. Particularly, the entry length (that is, the distance from the inlet boundary required to establish fully-developed flow) is maximum if uniform distributions are imposed at the inlet, as it was done in the present study as well as in most of the earlier ones reported in the literature.

However, the domain lengths defined by the different authors spanned over a wide range of sizes. In many cases, about 50 D to 60 D were simulated [26–29, 40–43]. In some studies, the length of the computational domain was kept fixed whilst varying D, resulting in different L/D ratios [23, 30]. Finally, other works considered much longer domains, e.g. 100 D in Refs. [35–38], $\approx 135D$ in Ref. [21], 200 D in Ref. [39], and $\approx 245D$ in Ref. [22]. Anyway, apart from few qualitative assessments [23, 41], it is not clear how the attainment of fully-developed flow was verified. For instance, Ling et al. [42] and Lin and Ebadian [43] simulated about 63 pipe diameters and, based on previous technical recommendations [60, 61], claimed that the entrance region is 50

D long. However, their own numerical results show that, even at 60 D from the inlet section, the volume fraction distribution meets the condition $\partial / \partial z = 0$ only roughly [43].

Fig 5. Development of different fluid dynamic quantities along direction z : (a) piezometric head and hydraulic gradient; (b) local solid volume fraction; (c) mean axial solid velocity; (d) axial slip velocity.

In order to provide clearer information, which can serve as guideline for future studies, a specific analysis of the development of the flow in the entrance region of the pipe was carried out, referring to the case V_{m}=3.0 m/s and $\langle \alpha_{\mathrm{s}} \rangle_A$=0.101 from dataset A. To this purpose, the domain was extended up to a length of 140 D, increasing the number of cells along direction z accordingly. The obtained results are depicted in Fig. 5. At first sight, the piezometric head, i.e. the ratio between the pressure and the specific weight of the liquid along the pipe axis, seems to linearly decrease over the whole pipe length, as characteristic of fully-developed flow (blue curve in Fig. 5a). A more detailed analysis, carried out by computing the axial derivative of the piezometric head, i.e. the hydraulic gradient, reveals that i_{m} stabilizes at about 50 D downstream of the inlet (red curve in Fig. 5a). The study was extended to three other fluid dynamic parameters, namely the concentration profile, the mean axial velocity profile of the solid phase, and the axial slip velocity profile, making reference to two specific positions along the vertical diameter, located 0.75 D and 0.25 D from the pipe bottom and referred to as A and B, respectively. Figures 5b-d clearly indicate that about 100 D of pipe are needed to completely stabilize these variables. At a distance from the inlet equal to 60 D, for instance, the values of α_{s} at positions A and B still differ some percent from the corresponding quantities at the outlet section (Fig. 5b), in line with the earlier findings of Lin and Ebadian [43]. Much larger deviations were detected for the axial slip velocity at position A. These results suggest that, depending on several factors (such as the employed computational model, the simulated flow conditions, and the required level of accuracy), about 50 D-60 D might not be enough for achieving a fully-developed slurry flow field. This justified the choice of setting the length of the domain to 120 D, considering the solution at 100 D suitable for comparison with the experiments.

3.3. Convergence of the calculations with respect to numerical parameters

An imperative requirement for obtaining reliable predictions is the convergence of the calculations with respect to the numerical parameters of the CFD model. In steady-state, Eulerian, cell-based models this essentially corresponds to verifying that the iteration algorithm has reached a stable solution and that such solution is grid-independent. The criteria employed to assess the convergence with respect to the iteration algorithm has already been explained at the end of Section 2.3, and this issue will not be further discussed hereafter. According to the authors' experience, when using commercial CFD codes, the reaching of convergence is strictly dependent upon specific features of the fluid dynamic model and the solution algorithm, which the user can control only partially. This makes it difficult to provide guidelines of general validity, which is the primary objective of the current study. The only general recommendation that could be made here is to apply proper under-relaxation to the momentum equations, as this strongly affects the overall convergence behavior. The assessment of the grid-independence is a non-trivial task even for a simple geometry like a straight pipe. Although most of the previous studies listed in Table 1 employed unstructured or block-structured meshes, the numerical simulations performed in this study, like those in [33, 35–38], relied on a discretization of the domain by means of fully-structured meshes in cylindrical-polar coordinates, as this type of grid is the natural choice and easy to generate in PHOENICS. The meshes were thus defined in terms of the number and the distributions of the subdivisions along the azimuthal, radial, and axial directions. As it is shown in Fig. 6, it was decided to keep the cells uniformly distributed along the azimuthal and axial direction, and to increase the level of discretization in the proximity of the pipe wall. Messa et al. [35, 36] detected a peculiar influence of the thickness of the near-wall layer of cells (referred to as 2δ in Fig. 3) on the predicted hydraulic gradient. Finally, they decided to set δ equal to 30 wall units, as this corresponds to having the lower bound of the log-law region in the center of the near-wall cells. The thickness 2δ was a priori estimated by the well known Blasius equation for fully-developed, turbulent, single-phase pipe flow

Fig 6. (a) three dimensional view of the computational mesh close to the inlet section; (b) detail of the discretization of the pipe section; (c) local magnification of the mesh close to the near-wall cells.

$$2\delta = 60\frac{\mu_l}{\rho_l V_m}\left[0.316\left(\frac{\rho_l V_m D}{\mu_l}\right)^{-0.25}\right]^{-0.5} \tag{33}$$

and the authors verified a posteriori that this value of 2δ broadly corresponded to 60 wall units in their slurry flow simulations. Once δ was defined, the distribution of the radial subdivisions was adjusted to create a smooth cell size transition over the pipe section. Note that, in these first works, the authors employed a built-in wall function method of PHOENICS to estimate the wall shear stress of the solid phase. Later, Messa and Malavasi [38] developed the wall boundary condition for the solid phase described in section 2.2 and implemented it in PHOENICS via user coding, but they adopted the same criterion for defining the size of the near-wall cells (Eq. 33). However, it is definitely desirable to overcome this criterion, which is awkward to apply in straight pipe flows (the mesh must be changed according to the value of the slurry bulk velocity, V_m), and very difficult to generalize to arbitrary flows.

To this purpose, an extensive grid sensitivity study was performed, again making reference to the case V_m=3.0 m/s and $\langle\alpha_s\rangle_A$=0.101 from dataset A. The analysis was divided in two stages, and it was extended to several fluid dynamics parameters characterizing the slurry mixture. However, for the sake of brevity, the results will be reported only for two quantities of great engineering interest, namely hydraulic gradient and concentration profile.

Table 3

Influence of the overall mesh resolution on the predicted hydraulic gradient. The right column represent the absolute deviation from the finest mesh solution (Grid 4).

Grid ID	N_θ [-]	N_r [-]	N_z [-]	i_m [-]	Δi_m [m/m]
Grid 1	20	20	200	0.075993	$-2\cdot10^{-6}$
Grid 2	30	30	200	0.075996	$1\cdot10^{-6}$
Grid 3	30	30	300	0.075991	$-4\cdot10^{-6}$
Grid 4	40	40	300	0.075995	-

Fig. 7. Influence of the overall mesh resolution on the predicted concentration profile: (a) chord-average concentration profiles computed on the different grids in Table 3; (b) absolute deviations from the finest grid solution (Grid 4).

In the first stage, the numbers of subdivisions along the azimuthal, radial, and axial directions (referred to as N_θ, N_r, and N_z, respectively) were varied keeping 2δ equal to 0.489 mm, the value obtained from Eq. 33. After running the simulations, the wall shear stress of the liquid phase was computed for all the near-wall cells, and the length δ could be converted to wall units, as follows

$$y^+ = \frac{\rho_l \delta \sqrt{\tau_l^w / \rho_l}}{\mu_l} \tag{34}$$

Finally, the y^+ values were averaged over all near-wall cells of the current slab, and this quantity, referred to as $\langle y^+ \rangle_\Gamma$, was found to be broadly constant for all meshes and equal to about 29.89. The numerical results highlighted no detectable influence of the overall number of cells on all inspected variables, as it is partially reported in Table 3 and Fig. 7 for hydraulic gradient and concentration profile. Based on these findings, from this point onwards N_θ, N_r, and N_z were set as in Grid 2, which produces absolute deviations from the finest grid solution of the order of 10^{-6} m/m for the hydraulic gradient (right column of Table 3) and lower than 0.002 for the chord-average concentration (Figure 7b).

Fig. 8. Influence of the thickness of the near-wall cells on the predicted hydraulic gradient (a) and the predicted concentration profile (b).

In the second stage, the focus was on the influence of the thickness of the near wall cells, 2δ, which was increased from 0.097 mm to 1.478 mm (corresponding to δ ranging from 0.049 mm to 0.739 mm, and to $\langle y^+ \rangle_\Gamma$ ranging from 5.98 to 90.7). As it is shown in Fig. 8, the numerical solution is practically unaffected by the value of $\langle y^+ \rangle_\Gamma$ for $\langle y^+ \rangle_\Gamma \geq 10.30$. The trend of the hydraulic gradient predictions in Fig. 8a) is different from that obtained by Messa et al. [36] using the built-in wall function, whereas it remained similar to the single-phase flow case. This result implies that the same mesh can be used for different flow conditions, provided that $\langle y^+ \rangle_\Gamma$ does not fall below a certain threshold within about 5 and 10. It is interesting to note also that, for the test case under consideration, such critically low values of $\langle y^+ \rangle_\Gamma$ produce near-wall cells that are

much smaller than the actual size of the solid particles and this is, in principle, inconsistent with the averaging procedure at the basis of the two-fluid model. Based on these findings, the remainder of the calculations was performed setting 2δ=0.8 mm, considerably larger than the particle size and corresponding to $\langle y^+ \rangle_\Gamma$ between 22 and 86 for all simulation scenarios.

3.4. Parametric sensitivity and calibration

All CFD models depend on a number of tuning parameters introducing inherent uncertainty to the solution. Generally, direct determination of these parameters via experiments is difficult, also because they might not even have a precise physical meaning. Instead, a common practice is to calibrate these terms all at once against the available experimental data which, in the case of slurry pipe flows, typically reduce to hydraulic gradient or concentration profile measurements. However, this procedure alone does not guarantee that the established values allow reliable prediction of other variables than those used to calibrate the model, nor that the same values are suitable outside the calibration range. A higher level of confidence could be achieved by assessing to what extent the different features of the solution are affected by the tuning constants before finding their optimal combination. This, in fact, would allow establishing the role played by each parameter, simplifying the calibration phase and making it more effective.

Indeed, some of the numerical investigations listed in Table 2 included a sensitivity studies with respect to some modelling features, such as the constitutive laws of the solid phase [21, 23, 40], the forces included in the interfacial momentum transfer term [23, 24], or the turbulence closures [24]. However, the findings appear difficult to generalize, in the sense that they are limited in terms of flow conditions, model parameters, or output variables. For these reasons, a more comprehensive analysis is shown hereafter.

The tuning constants of the β-σ model have been identified as β, σ, and the dimensionless factors of the k-ε standard turbulence model, namely, σ_k, σ_ε, $C_{1\varepsilon}$, $C_{2\varepsilon}$, and C_μ. Since the values of these last variables have been well established since many decades, at least for single-phase flow, they were not subject of investigation, and the focus was turned to β and σ. Actually, the use of the k-ε standard turbulence model instead of other options (such as k-ε RNG, k-ε Realizable, k-ω SST) might be regarded as a source of uncertainty in the numerical results. However, preliminary tests confirmed the expectation that the superior

performance of turbulence models other the k-ε standard is not so evident for straight pipe flows, thereby leading to the decision of not deepening into this feature of the TFM. Similarly, the effect of the choice of the equation relating C_d to Re_m was explored, but soon it was realized that replacing the analog of the Schiller and Naumann formula (Eq. 9) with alternative correlations (e.g., Clift et al. [62], Turton and Levenspiel [63]) produced no significant changes to the numerical solution. This occurred because, for the simulated flow conditions, the values of Re_m varied approximately between 0.005 and 5, and all the above formulas produce very similar C_d estimates in such range of Reynolds numbers.

Three combinations of β and σ were considered for all simulation scenarios, and the effect of these parameters on different output variables was investigated. For each dataset, the range of variation of β was defined around the recommendations of the ealier paper [38], namely, β equal to 1.5, 3.0, and 3.3 for glass beads, regular sand, and highly sharp sand, respectively, and σ equal to 0.7.

Fig. 9. Effect of β and σ on the predicted chord-average solid volume fraction profile for different simulation scenarios. The experimental data discussed in Refs. [56–58] are reported too, including the two sets of repeatibility measurements made in dataset B.

The influence exerted by β and σ on the predicted chord-averaged concentration profile was found to be similar for all simulation scenarios but, for space reasons, it is shown in Fig. 9 only for two representative cases of each of the three datasets. Anyway, the numerical data might be provided to the interested reader for these and all other testing conditions upon request to the corresponding author. Two considerations can be drawn. First, either a decrease in σ or an increase in β produces a flatter concentration profile. This behavior might be interpreted by considering that a lower σ results in higher diffusivity in the mass conservation equations (Eqs. 1,2), whereas a higher β brings about a higher μ_m (Eq. 6) and, in turn, stronger inter-phase friction (Eqs. 8-10). Second, the influence of β is very weak for low values of $\langle \alpha_s \rangle_A$ but gets stronger as the slurry becomes denser. This might be a consequence of the greater role played, in the β-σ model, by the interfacial momentum transfer term for highly concentrated mixtures.

Fig. 10. Hydraulic gradient versus slurry velocity for some representative simulation scenarios: numerical predictions for different combinations of β and σ, expeirmental data reported in [56–58] (including the two sets of repeatibility measurements made in dataset B), and curve for single-phase flow. The values or range of values of deposition-limit velocities indicated by the experimenters have also been reported.

Fig. 11. Parity plots of predicted versus measured hydraulic gradients for all simulation scenarios from datasets A, B, and C: effect of β and σ on the numerical estimates. For dataset B, the experimental data are the average over the two repeatability measurements. Only the data fulfilling the conditions set out later in Section 3.7 have been included in the plots.

The sensitivity analysis was then focused on the hydraulic gradient. The V_m-i_m curves in Fig. 10 indicate that, whilst σ has very little effect on the i_m predictions, β plays a role in affecting the energy dissipations of dense slurries. This has been explained by observing that, unlike σ, β has a direct effect on the wall shear stress of the solid phase (via Re_s^w, Eq. 28) which is the main responsible for the additional friction due to the particles.

Fig. 12. The plot illustrates the meaning of φ, which is the slope angle of the linear regression line through the chord-average concentration values within $0.3 \le y/D \le 0.7$.

If experimental data are available for concentration profile and hydraulic gradient, β and σ can be calibrated to match the measurements. The considerations above open the way to a decoupled procedure, involving, first, the tuning of β with respect to the hydraulic gradient data and, then, the calibration of σ on the concentration measurements. However, translating this concept into a concrete strategy is not straightforward. In fact, whilst the level of agreement between computed and measured i_m-values is quantitatively perceivable by parity plots like those in Fig. 11, and it can be reduced to a single scalar by referring to the Mean Absolute Percentage Error (MAPE)

$$\mathrm{MAPE}\left(i_{\mathrm{m}}\right)=\frac{100}{N}\sum_{j=1}^{N}\left|i_{\mathrm{m},j}^{\mathrm{num}}-i_{\mathrm{m},j}^{\mathrm{exp}}\right|\cdot\frac{2}{i_{\mathrm{m},j}^{\mathrm{num}}+i_{\mathrm{m},j}^{\mathrm{exp}}} \tag{35}$$

the same approach cannot be directly applied to a one-dimensional array such as the chord-average concentration profile. However, in the flows considered in this article, the slope of the chord-average concentration profile is almost constant in the bulk region of the pipe and, therefore, it can be fairly well represented by the linear regression slope angle of the $\langle\alpha_{\mathrm{s}}\rangle_{\gamma}$ vs y/D points within $0.3\le y/D\le 0.7$, referred to as φ (Fig. 12). The particular shape of the concentration profile enables the possibility to quantify the accuracy of the β-σ model in predicting the concentration distribution by calulating, for instance, the Mean Absolute Error (MAE) of φ:

$$\mathrm{MAE}\left(\varphi\right)=\frac{1}{N}\sum_{j=1}^{N}\left|\varphi_{j}^{\mathrm{num}}-\varphi_{j}^{\mathrm{exp}}\right| \tag{36}$$

Table 4

Absolute error statistics on hydraulic gradient and concentration profile slope angle for datasets A to C and different combinations of β and σ. Only the data fulfilling the conditions set out later in Section 3.7 have been included in the calculation.

Dataset ID	β [-]	σ [-]	MAPE(i_{m}) [%]	MAE(φ) [°]
A	1.0	0.7	2.58	2.41
	1.5	0.7	2.77	2.12
	1.0	0.5	2.47	2.31
B	2.0	0.7	7.31	1.23
	3.0	0.7	8.60	1.71
	2.0	1.0	7.16	1.30
C	4.0	0.7	2.81	1.34
	3.0	0.7	7.95	1.36
	4.0	0.5	2.92	1.83

In principle, one could try to identify the combination of β and σ which minimizes the MAPE of i_{m} and the MAE of φ. Although conceptually simple, this approach raises a number of practical issues, related with the uncertainty of the calibration data as well as the sophisticated

algorithms and considerable computational effort required even with a fast-to-solve model such as the β-σ one. The development of an effective automated calibration procedure could be a possible suggestion for future research. In the current paper, a simpler approach is followed, consisting in identifiying a reasonably good combination of β and σ among the three considered in the sensitivity analysis previously discussed. This was primarily achieved by graphically inspecting the concentration profiles (Fig. 9) and the hydraulic gradient versus slurry velocity curves (Fig. 10). Then, the hydraulic gradient parity plots (Fig. 11) and the statistical indexes MAPE(i_m) and MAE(φ) (Table 4) allowed for a quantitative assessment of the level of agreement between experiments and compuations.

It is worth noting that, as Figs. 10b,d suggest, the β-σ model is no longer accurate when the mixture velocity approaches the deposition limit value, resulting in a strong underestimation of the hydraulic gradient. A detailed discussion on this aspect will be provided in Section 3.7 but, for the moment, it is enough to underline that the data not fulfilling the established conditions of applicability of the β-σ model do not appear in the parity plots and they were not included in the calculation of the statistical indexes.

The combinations of β and σ considered in the remainder of the paper were (1.0, 0.5), (2.0, 1.0), and (4.0, 0.7) for datasets A, B, and C, respectively, which result in relatively low average absolute errors on i_m and φ. Although these pairs of values cannot be regaded as optimum in an absolute sense, and might be refined and improved, they produce numerical results in reasonable agreement with the experiments, as the reader can easily realize by looking at Figs. 9-11 and Table 4.

The study described above indicates that, provided that β and σ have been properly tuned, the TFM is capable of accurately reproducing the chord-average concentration profile and the hydraulic gradient. Furhermore, generalizing the earlier findings in [35, 36, 38], it was observed that increasing σ to 1.0 from the suggested 0.7 might improve the predictive capacity in some cases, and that the optimum values of β might differ from the recommendations in Messa and Malavasi [38]. Finally, establishing β as 2.0 and 4.0 in datasets B and C, respectively, indicates that this parameter is not just related with the particle shape, as argued in Ref. [38], but it needs more complex characterization. The implication of this aspect on the use of the model for predictive and extrapolation purposes will be subject of discussion in Section 3.6.

3.5. *Critical analysis of difficult-to-measure quantities*

Once the role played by the tuning parameters on the different features of the numerical solution has been assessed through a sensitivity analysis, and a reasonable combination of their values has been established, the TFM can be used to attain information about the slurry flow that cannot be provided (at least easily) by experiments. For instance, the wall shear stress of the two phases is very relevant, being connected with both the energy dissipation and other phenomena such as pipe wall abrasion.

Fig. 13. (a-e) distribution of the wall shear stress for five simulation scenarios from dataset B (blue curve: liquid phase; red curve: solid phase; black curve: sum of liquid and solid phases). The normalization factor $\tau_{\mathrm{ref}}^{\mathrm{w}}$ is given in Eq. 38; (f) chord-average volume fraction profiles for the same test cases.

Figures 13a-e show the distributions of $\tau_{\mathrm{l}}^{\mathrm{w}}$ and $\tau_{\mathrm{s}}^{\mathrm{w}}$ over the pipe circumference for five representative cases from dataset B. These profiles are linked with the hydraulic gradient, since it can be proven that, in the fully-developed flow region,

$$\rho_{\mathrm{l}} \,|\, \boldsymbol{g} \,|\, i_{\mathrm{m}} \left(\pi \frac{D^2}{4} \right) = \frac{D}{2} \int_0^{2\pi} \left(\tau_{\mathrm{l}}^{\mathrm{w}} \alpha_{\mathrm{l}}^{\mathrm{w}} + \tau_{\mathrm{s}}^{\mathrm{w}} \alpha_{\mathrm{s}}^{\mathrm{w}} \right) d\theta \tag{37}$$

where $\alpha_{\mathrm{l}}^{\mathrm{w}}$ and $\alpha_{\mathrm{s}}^{\mathrm{w}}$ are the local volume fractions of the phases at the wall. The fulfillment of Eq. 37 is fundamental to give confidence to the wall shear stress predictions. To underline this relation and make it possible to compare different scenarios, the results presented in Figs. 13(a-e) have been normalized by

$$\tau_{\mathrm{ref}}^{\mathrm{w}} = \frac{\frac{D}{2} \int_0^{2\pi} \left(\tau_{\mathrm{l}}^{\mathrm{w}} \alpha_{\mathrm{l}}^{\mathrm{w}} + \tau_{\mathrm{s}}^{\mathrm{w}} \alpha_{\mathrm{s}}^{\mathrm{w}} \right) d\theta}{\pi D} = \rho_{\mathrm{l}} \,|\, \boldsymbol{g} \,|\, i_{\mathrm{m}} \frac{D}{4} \tag{38}$$

The circumferential wall shear stress profiles show an evident analogy with those of the near-wall volume fraction distributions. In fact, the solid wall shear stress is maximum at the bottom of the pipe, whereas that of the liquid phase assumes the highest value at the top. As the mixture velocity increases for a given area-averaged concentration, the flow regime tends to become

pseudo-homogeneous suspension (Fig. 13f), and, accordingly, the two τ^{w} -profiles evolve towards an axi-symmetrical configuration (Figs. 13a-c). A similar effect is observed as the solid loading increases whilst the mixture velocity remains the same (Figs. 13a,d,e), because of the increased phase coupling and within-phase diffusion. It is also noted that the relative contributions of the two phases to the total wall shear stress significantly changes with the amount of solids in the slurry, the major role being played by τ_{l}^{w} for $\langle\alpha_{s}\rangle_{A} \approx 0.13$, and by τ_{s}^{w} for $\langle\alpha_{s}\rangle_{A} \approx 0.35$.

Fig. 14. Axial velocity profile of the mixture along the vertical pipe diameter for three different scenarios from dataset B (continuous lines: simulations with τ_{s}^{w} from Eq. 26; dotted lines: simulations with $\tau_{s}^{w}=0$). The points of maximum $U_{m,z}$ are highlighted in the plot.

Another feature of slurry flows which is rather hard to determine experimentally, but can be easily obtained by means of a CFD simulation, is the velocity field. The available measurements reported in the literature (e.g., [25, 58, 64–67]) agree that the maximum velocity is located in the upper part of the pipe, this effect being hardly visible for pseudo-homogeneous flow but becoming more and more enhanced as the vertical concentration gradient increases. As it is proven in Fig. 14, in which $U_{m,z}$ was calculated as

$$U_{m,z} = \frac{U_{l,z}\rho_{l}\alpha_{l} + U_{s,z}\rho_{s}\alpha_{s}}{\rho_{l}\alpha_{l} + \rho_{s}\alpha_{s}} \tag{39}$$

the solution of the β-σ model is physically consistent. This capability is closely bound to the correct evalulation of the wall shear stress of the solid phase, and, for instance, is no longer achieved if τ_{s}^{w} is neglected. Being capable of capturing the upward shift of the maximum velocity represents an essential requirement to guarantee the reliability of a TFM.

Fig. 15. Distribution of the in plane velocity vectors of the solid phase, colored by their magnitude, for case $V_{m} = 2.3$ m/s and $\langle\alpha_{s}\rangle_{A} = 0.11$ from dataset A. The corresponding chord average volume fraction profile is shown in Fig. 9a.

The velocity field predicted by the β-σ model is strongly related with the presence of

the diffusion fluxes in the phasic continuity equations (Eqs. 1,2). In fact, in the fully developed flow region, the absence of such fluxes would result in

$$\int_{\gamma} \rho_{\mathrm{s}} \alpha_{\mathrm{s}} U_{\mathrm{s},y} dx = 0 \tag{40}$$

$$\int_{\gamma} \rho_{\mathrm{l}} \alpha_{\mathrm{l}} U_{\mathrm{l},y} dx = 0 \tag{41}$$

as it can be proven by imposing the mass conservation of both phases to a control volume bounded by the pipe wall and an arbitrary horizontal plane, the chord width being γ (Fig. 4). Since all terms in the equations above are positive expect for $U_{\mathrm{l},y}$ and $U_{\mathrm{s},y}$, these terms must change their sign along each horizontal chord γ, yielding self-balanced in-plane advection fluxes. This is no longer true in the β-σ model, because the balance of the in-plane mass fluxes involves both the advective and the phase diffusion terms. Since the solid volume fraction decreases along the y-direction owing to the effect of gravity (that is, $\partial \alpha_{\mathrm{s}} / \partial y < 0$), the phase diffusion fluxes of the solid phase are likely to be directed upwards, making a distribution of in-plane velocity vectors all directed downwards, like that shown in Fig. 15, consistent with the mass conservation principle.

A TFM formulation including phase diffusion fluxes has considerable advantages in terms ease in attaining convergence to a smooth solution without spurious oscillations. At the same time, it makes the physical interpretation of the velocity field less clear. Indeed, $\boldsymbol{U}_k$ might be clearly associated with the advection flux per unit area, $\rho_k \alpha_k \boldsymbol{U}_k \cdot \boldsymbol{n}$, but it appears rather difficult to relate the in-plane vectors depicted in Fig. 15 with the actual movement of the solid phase. Nevertheless, in fully-developed pipe flows, in-plane velocity components are very small compared to the axial one, and the phase diffusion fluxes are zero along the flow direction (since $\partial \alpha_k / \partial z = 0$); therefore, it seems reasonable to compare the $U_{\mathrm{m},z}$ (Eq. 39) profiles with the experimental measurements.

Fig. 16. Modulus of the slip velocity, averaged over the circumference depicted in Fig. 15 ad divided by the bulk-mean velocity, for datasets A to C.

On the other side, the issue becomes significant when referring to the slip velocity, $\boldsymbol{W} = \boldsymbol{U}_{\mathrm{l}} - \boldsymbol{U}_{\mathrm{s}}$, since, for the flow conditions addressed in this study, this quantity is small and

dominated by the in-plane components. Based on the reasons discussed above, the presence of phase diffusion fluxes prevents the possibility of relating the $\boldsymbol{W}$ predictions to the actual velocity difference between the solids and the carrier fluid, or to the conveying capacity. Surely, $\boldsymbol{W}$ is associated with the exchange of momentum between the two phases: this variable, in fact, is needed to calculate the interfacial momentum transfer term, $\boldsymbol{M}$ (Eq. 8). Note that the modulus of $\boldsymbol{W}$ appears also in the definition of the modified particle Reynolds number, Re_{m} (Eq. 10), which is used to compute the drag coefficient.

The dependence of $\boldsymbol{W}$ upon the bulk-mean velocity and the area-averaged concentration is shown in Fig. 16 for datasets A to C. In the three plots, the average modulus of $\boldsymbol{W}$ over the circumference Π highlighted in Fig. 15, normalized by the bulk-mean velocity, was used as an indicator of the slip. For all datasets, $\langle|\boldsymbol{W}|\rangle_{\Pi}/V_{\mathrm{m}}$ decreases as either V_{m} or $\langle\alpha_{\mathrm{s}}\rangle_{A}$ increases, indicating that the two phases become increasingly coupled as the slurry gets denser or flows faster. This conclusion is further confirmed by the fact that, under these conditions, the solids tend to be uniformly distributed over the pipe section, and the velocity profile becomes axisymmetric, further demonstrating the physical consistency of the β-σ model solution.

3.6. Prediction of slurry flows in larger pipes

Many industrial applications require pipes substantially larger than 150 mm. It is of utmost importance to assess whether the β-σ model can be a useful predictive tool in these situations, especially if no measurements are available for tuning the empirical constants β and σ. The PhD thesis of Gillies [59] gives the possibility to address this issue, since, as already summarized in Table 2, it provides experimental data for broadly the same type of fine-sand slurries (d_{p}=0.180 mm) flowing in pipes with diameters of 53.2 mm and 495 mm. A two-step procedure was carried out for testing the pipe size-up scalability of the β-σ model.

Fig. 17. Effect of β and σ on the predicted chord-average solid volume fraction profile for dataset D1.

Fig. 18. Effect of β and σ on the hydraulic gradient vs velocity predictions for dataset D1.

Fig. 19. The parity plots of predicted versus measured hydraulic gradients for dataset D1 and different combinations of β and σ.

At first, following the same approach illustrated in Section 3.4, proper values of β and σ were determined for the 53.2-mm diameter pipe experiments by considering three different combinations of the two parameters, namely (3.0, 0.7), as recommended in Ref. [38], (2.0, 1.0), as in dataset B, and (4.0, 0.7), as in dataset C. All tests reported in Ref. [59] for the 53.2-mm diameter pipe were reproduced, except those with $\langle \alpha_s \rangle_A = 0.45$ since, in these cases, interparticle collisions play a significant role and the flow is unlikely to be fully-suspended (see Section 3.7). The results of the sensitivity analysis, shown in Figs. 17-19, indicate that setting β=2.0 and σ =1.0 produces reasonably accurate predictions of concentration profile and hydraulic gradient for dataset D1. Note that, this time, no calculation of MAE(φ) was performed, since the statistics based on four data only would have not been so significant.

Fig. 20. Validation of the model on dataset D2. Comparison between predicted and measured chord-average concentration profiles (a,b) and hydraulic gradient versus slurry velocity curves (c). Parity plot of predicted versus measured hydraulic gradient for all flow conditions above the deposition limit velocity.

Afterwards, the same combination of tuning parameters was employed to simulate the experiments in the 495-mm diameter pipe. Only two concentration profiles were reported in Gillies [59] above the deposition-limit velocity, and the predictions of the β-σ model are in fairly good agreement with both of them Fig. 20(a,b). Conversely, much more hydraulic gradient data are available, and, as seen in Fig. 20(c,d), the capability of the TFM to predict this parameter is highly satisfactory: excluding the flow conditions in which the experimenter detected the occurrence of solid deposit, the MAPE of all i_m estimates was as low as about 3.50%.

The scarcity of experimental data on slurry flows in large diameter pipes did not allow a complete assessment of the pipe size-up scalability of the model, a topic which is definitely recommended for future study. Nevertheless, the preliminary analysis described in this section

gives some confidence that, after calibration on experiments in a small pipe at the laboratory scale, the β-σ model can be used to simulate the behavior of the same type of particles flowing in bigger pipes.

3.7. Conditions for the applicability of the β-σ model

As one of the guiding principles in modelling, the applicability domain of the β-σ model was properly defined, paying special attention to turning the applicability conditions into criteria which can be easily verified, ideally - if possible - before running any simulation.

Fig. 21. Parity plot comparing the actual values of d_p^+ obtained from the numerical simulations with the a priori estimate given Eq. 42. The horizontal bars denote the actual variability of d_p^+ along the pipe circumference, and the markers indicate the mean values.

A first condition to be satisfied is related with the use of Eq. 27 for calculating the wall shear stress of the solid phase since, as already mentioned, this model requires d_p^+ to be smaller than 30. In principe, this condition can be verified only a posteriori, since d_p^+ depends on the friction velocity of the liquid phase, which is an output of the numerical simulation. Furthermore, d_p^+ varies along the pipe wall, and, as shown in Fig. 21, a rough overestimation of this quantity can be obtained by dividing d_p by the wall-unit determined by applying Blasius's formula for turbulent single-phase pipe flow. Such estimate, referred to as d_p^{+B}, can be calculated a priori as

$$d_p^{+B} = \frac{d_p}{\frac{\mu_l}{\rho_l V_m}\left[0.316\left(\frac{\rho_l V_m D}{\mu_l}\right)^{-0.25}\right]^{-0.5}} \tag{42}$$

The constraint $d_p^{+B} < 30$ allows determining a priori whether the condition $d_p^+ < 30$ is fulfilled and, therefore, whether the β-σ model is applicable. Note that, for all flow conditions addressed in this study, $d_p^+ > 5$ and, therefore, the particles are not entirely embedded in the viscous sublayer.

Table 5

Experimentally observed deposition-limit velocities and predictions of the correlation of Thomas [11]. The two V_{dl}^{exp} intervals in datasets D1 and D2 correspond to transitions between stationary and intermittent deposit and between intermittent and no deposit, respectively.

Dataset ID	$\langle \alpha_s \rangle$ [-]	V_{dl}^{exp} [m/s]		V_{dl}^{T} [m/s]
A	≈ 0.11	$1.48 \div 1.76$		$1.33 \div 1.62$
	≈ 0.18	$1.51 \div 1.74$		
	≈ 0.26	$1.22 \div 1.45$		
	≈ 0.38	$1.24 \div 1.50$		
B	≈ 0.13	1.80		$1.56 \div 1.91$
	≈ 0.25	1.70		
	≈ 0.34	1.55		
C	≈ 0.19	1.10		$0.96 \div 1.18$
	≈ 0.24	1.00		
	≈ 0.29	1.05		
	≈ 0.33	1.15		
D1	0.15		$1.37 \div 1.52$	$1.27 \div 1.40$
	0.30	$1.10 \div 1.22$	$1.52 \div 1.83$	
D2	0.10	$3.11 \div 3.20$	$3.51 \div 3.66$	$2.46 \div 3.00$
	0.15	$3.02 \div 3.20$	$3.51 \div 3.66$	
	0.20	$3.05 \div 3.20$	$3.51 \div 3.66$	
	0.25	$2.93 \div 3.05$	$3.34 \div 3.49$	
	0.29	$2.74 \div 2.83$	$3.35 \div 3.51$	
	0.29	$2.65 \div 2.74$	$3.51 \div 3.66$	

Other conditions arise from the need to guarantee that the flow is fully suspended. This primarily implies that no solid deposit must occur at the bottom of the pipe, and therefore, that V_m exceeds the deposition-limit velocity, V_{dl}. Since no prediction of V_{dl} is achievable with the β-σ model, it was explored whether any of the correlations available in the literature could be

employed to define an application constraint. Particularly, the focus was on the formula for V_{dl} recently proposed by Thomas [11], which substantially covers the range of testing conditions considered in this study and reads as follows:

$$V_{dl}^{T} = F_L \sqrt{2 |\boldsymbol{g}| D \left(\frac{\rho_s}{\rho_l} - 1 \right)} \tag{43}$$

$$F_L = 2 + 0.305 \log_{10}\Delta + 1.1 \cdot 10^{-4} \Delta^{-0.489} - 0.044 \left(10^7 \Delta\right)^{-1.06} \tag{44}$$

$$\Delta = \frac{3}{4} \frac{\rho_l w_t^2}{|\boldsymbol{g}| D (\rho_s - \rho_l)} \tag{45}$$

where w_t is the terminal settling velocity of a particle falling in a quiescent liquid, which can be evaluted from the following equation:

$$w_t^2 = \frac{4}{3} \left(\frac{\rho_s}{\rho_l} - 1 \right) \frac{|\boldsymbol{g}| d_p}{C_d} \tag{46}$$

Note that C_d depends on w_t through the Shiller and Naumann correlation [49] and the particle Reynolds number $d_p w_t \rho_l / \mu_l$; therefore, Eq. 46 must be solved iteratively.

For all datasets, the values or ranges of V_{dl} reported by the experimenters have been compared against the predictions of the Thomas' correlation, which have been attributed a variability of ±10% as recommended in Ref. [11] to account for the influence of solid concentration. The results, summarized in Table 3, indicate that, although with some degree of understimation for dataset D, the Thomas model provided a fairly good estimation of the deposition-limit velocity observed in the experiments and, thus, V_{dl}^{T} was considered an adequate parameter to develop an a priori applicability condition.

Fig. 22. Deviation of experimentally determined hydraulic gradient as a function of the V_m / V_{dl}^{T} ratio for all numerical simulations. The values of β and σ were those determined after the sensitivity analysis previously illustrated.

As Figs. 10b,d and 19 suggest, the β-σ model might tend to underpredict the hydraulic gradient close to or below the deposition-limit velocity. Starting from these considerations, the

percentage deviation between predicted and measured hydraulic gradient was graphically represented as a function of the V_m / V_{dl}^T ratio for all the simulated flow conditions, suggesting that $V_m > 1.5 V_{dl}^T$ could be a sufficiently conservative validity constraint (Fig. 22).

A third limit to the applicability of the β-σ model is due to the fact that, as already mentioned at the beginning of the paper, slurry flows with mean solids concentration exceeding of about 0.40 are primarily dominated by particle-particle contacts and cannot be classified as fully-suspended. The β-σ model has not been designed for application to such dense slurries and, therefore, the authors' recommendation is to disregard solutions with local values of α_s above about 0.45. Unfortunately, strictly speaking, this condition can be verified only a posteriori.

As a final note, it is recalled that, in the present study, the β-σ model has been tested in the following conditions, namely, pipe diameter from 53.2 to 495 mm, area-averaged solid volume fractions between about 0.10 and about 0.36, slurry velocities between about 1.10 m/s and about 6.0 m/s (corresponding to V_m / V_{dl}^T ratios in the approximate range 0.8-3.5). As far as the type of particles are concerned, the investigation was mainly focused on natural sands with 2650 kg/m^3 density and size ranging from 0.090 to 0.180 mm, but also spherical glass beads with 2450 ^{3} density and 0.180 mm size were successfully explored.

4. Conclusion

This paper focuses on the application of the Two Fluid Model for the engineering simulation of liquid-solid slurry pipe flows, considering the relevant benchmark of straight horizontal pipe. An extensive literature survey of previous numerical investigations of slurry flows in horizontal pipes was carried out first (Table 1). Compared to other modelling approaches (Fig. 1), the TFM allows the best compromise between the computational cost and the capability to capture the physical mechanisms governing slurry pipe flows, revealing a tool capable of satisfying essential engineering requirements. At the same time, several numerical and modelling factors affect the simulation results, making the comparison against experiments essential but not sufficient to guarantee the reliability of the predictions outside the specific calibration range.

Based on these considerations, in the first part of the paper it was decided to gather further insight into these dependencies, with the goal of providing best practice guidelines for future

academic and professional use of the TFM for slurry flow modelling. The proper definition of the computational domain, the verification of the numerical convergence, the identification of the model constants and the assessment of their role, and their calibration based on experimental findings were carefully explored. In performing this study, reference was made to the TFM previously developed by one of the authors of the paper, here renamed as the β-σ model to highlight the existence of two main tuning parameters. Anyway, it was tried to give indications relevant also for other TFMs. For the sake of generality and strength of the drawn conclusions, three different datasets were considered for the experimental verification of the model, resulting in 108 different simulation scenarios covering a wide range of pipe diameters, solid concentrations, and slurry velocities (Table 2). Although only fine particles could be investigated, some exploration of the effects of particle material and size was allowed. Main conclusions are as follows.

- Particular attention must be paid to the definition of the length of the computational domain needed to achieve fully developed flow, which is strictly connected to the parameter subject of investigation, alongside with the type of imposed boundary conditions. Lengths of about 50-60 diameters are suitable to attain reliable predictions of hydraulic gradient and mean velocity profile, but might not be enough to attain complete development of the concentration profile and the slip velocity from uniform inlet distributions (Fig. 5). Apparently, 100 diameters allow the most accurate modeling.
- The spatial discretization of the domain must be done carefully, since some features of the computational mesh, such as the thickness of the near-wall cells, might produce adverse effects on the hydraulic gradient estimates. This behavior seems connected with the type of wall boundary condition for the solid phase implemented in the model, as it can be inferred by comparing the results of the present investigation with those of earlier papers [35, 36].
- It is fundamental to identify and establish the role played by the tuning parameters of the TFM by analyzing the influence on all output quantities of interest, thereby developing efficient calibration strategies. Here it was found that σ affects the concentration profiles but it has practically no effect on the hydraulic gradient, whereas β showed an opposite behavior for low particle loading (Figs. 9 and 10).
- Combinations of β and σ providing overall good agreement with the experimental data were determined for the three datasets, suggesting that these two parameters reflect not

only the influence of particle material, as guessed in Ref. [38], but also other features of the testing conditions.

In the second part of the paper, the model has been employed for determining difficult-to-measure characteristics of slurry pipe flows in the calibration range. This analysis not only resulted in an additional check list for the TFM reliability, but also determined the potential of the β-σ model as a tool to get further insight into the physical phenomenon and its engineering implications. The key findings are summarized below.

- The TFM could be used to obtain the distribution of the wall shear stresses of the two phases over the pipe walls, which is not only connected with the energy losses but also with other phenomena like abrasion (Fig. 13). As an additional check on the reliability of the numerical estimates, the fulfillment of the integral mixture momentum balance (Eq. 37) might be verified. Additionally, the wall shear stress profiles must be physically consistent, in that the influence of bulk-mean velocity and solids concentration must be properly justified.
- The TFM must be capable of predicting the shift of the maximum velocity towards the pipe crown, which was well confirmed by the experimental evidence and properly justified from a physical point of view. The capability of the β-σ TFM in capturing this effect seems related with the type of wall boundary condition imposed to the solid phase (Fig. 14).
- The nature of the in-plane velocity components must be carefully established, particularly in the presence of phase-diffusion fluxes (Fig. 15). This feature has a direct influence on the momentum transfer between the phases, governed by the slip velocity. The physical consistency of the slip velocity as a function of bulk-mean velocity and solids concentration might provide further confirmation to the model's reliability (Fig. 16).

Finally, the last part of the article was aimed at strengthening the application impact and usability of the β-σ TFM. Particularly:

- It was suggested that, once β and σ are calibrated with respect to measurements in a small pipe at the laboratory scale, the same values allow for fairly good predictions of the behavior of the same type of particles flowing in bigger pipes, which are definitely harder to test experimentally (Figs. 17 to 20).

- Three specific and quantitative conditions for the applicability of the β-σ model have been indicated (Section 3.7). Two of them can be easily assessed before running any simulation. The fulfillment of the third condition can be reasonably expected but, strictly speaking, it can be established only once the numerical solution has been calculated.

Many features of the β-σ model shall make it worthy of interest for scientific research and engineering purposes. However, two unresolved issues require further study, and they are left as recommendation for future improvement. Firstly, the applicability domain of the model is limited by several constraints (above all, on the size of the particles), thereby precluding its use for addressing many types of slurry flows frequently encountered in the industrial applications. Secondly, the model is not capable of providing estimates of the deposition-limit velocity, which, alongside with the hydraulic gradient, is probably the second most important requirement for slurry pipeline design.

Acknowledgements

Authors would like to acknowledge Dr. Randall Gillies of Saskatchewan Research Council for making his experimental data available for use in this research, and Dr. Michael Malin from CHAM Limited for the useful support, comments, and discussion. The research at the Institute of Hydrodynamics in Prague was supported by the Czech Academy of Sciences (project RVO 67985874).

References

[1] P. Doron, D. Barnea, Flow pattern maps for solid-liquid flow in pipes, Int. J. Multiphase Flow 22 (1996), 273–283.

[2] A.C. Korving, High concentrated fine-sand slurry flow in pipelines: experimental study, Proc. 15 th Int. Conf. Hydrotransport, 2002.

[3] K.C. Wilson, G.R. Addie, A. Sellgren, R. Clift, Slurry transport using centrifugal pumps, Springer, New York, 2006.

[4] K.C. Wilson, A unified physically-based analysis of solid-liquid pipeline flow, Proc. Hydrotransport 4, BHRA, Cranfield, UK, 1976, pp. 1-16.

[5] P. Doron, D. Barnea, A three-layer model for solid-liquid flow in horizontal pipes, Int. J. Multiphase Flow 19 (1993), 1029–1043.

[6] V. Matoušek, J. Krupička, M. Kesely, A layered model for inclined pipe flow of settling slurry, Powder Technol. 333 (2018), 317–236.

[7] K.C. Wilson, D.G. Judge, New techniques for the scale-up of pilot plant results to coal slurry pipelines, Proc. Int. Symp. on Freight Pipelines, 1976.

[8] K.C. Wilson, D.G. Judge, Analytically based nomographic charts for sand water flow, Proc. 5th Int. Conf. Hydraulic Transport of Solids in Pipes, 1978.

[9] A. Thomas, Predicting the deposit velocity for horizontal turbulent pipe flow of slurries, Int. J. Multiphase Flow 5 (1979), 113–129.

[10] R.S. Sanders, R.G. Gillies, M.J. McKibbon, C. Litzenberger, C.A. Shook, Deposition velocities for particle of intermediate size in turbulent flow, Proc. 16th Int. Conf. Hydrotransport, 2004.

[11] A. Thomas, A modification of the Wilson & Judge deposit velocity equation, extending its applicability to finer particles and larger pipe sizes, Proc. 17th Int. Conf. Transport and Sedimentation of Solid Particles, 2015.

[12] A. Uzi, A. Levy, Flow characteristics of coarse particles in horizontal hydraulic conveying, Powder Technol. 326 (2018), 302–321.

[13] V. Matoušek, M. Kesely, R. Visintainer, A. Sellgren, Pipe friction of bimodal settling slurry flow, Proc. 9th Int. Conf. Conveying and Handling of Particulate Solids, 2018.

[14] C.T. Crowe, J.D. Schwarzkopf, M. Sommerfeld, Y. Tsuji, Multiphase flows with droplets and particles, CRC Press, Boca Raton, US-FL, 2012.

[15] M. Manninen, V. Taivassalo, S. Kallio, On the Mixture Models for Multiphase Flow, VTT Publications, Espoo, 1996.

[16] J.C. Goeree, G.H. Keetels, E.A. Munts, H.H. Bugdayci, C. van Rhee, Concentration and velocity profiles of sediment-water mixtures using the drift-flux model, Can. J. Chem. Eng. 94 (2016) 1048–1058.

[17] J. Capecelatro, O. Desjardins, Eulerian-Lagrangian modeling of turbulent liquid-solid slurries in horizontal pipes, Int. J. Multiphase Flow 55 (2013), 64–79.

[18] S.K. Arolla, O. Desjardins, Transport modeling of sedimenting particles in a turbulent pipe flow using Euler-Lagrange large eddy simulation, Int. J. Multiphase Flow 75 (2015), 1–11.

[19] H.K. Versteeg, W. Malalasekera, An Introduction to Computational Fluid Dynamics: The Finite Volume Methods, Pearson Prentice Hall, Harlow UK, 2007.

[20] A.D. Burns, T. Frank, I. Hamill, J.M. Shi, The Favre Averaged Drag Model for Turbulent Dispersion in Eulerian Multi-Phase Flows, Proc. 5th International Conference on Multiphase Flow ICMF2004, 2004, Paper No. 392.

[21] F.H. Hernández, A.J. Blanco, L. Rojas-Solórzano, CFD modeling of slurry flows in horizontal pipes, Proc. ASME 2008 Fluids Engineering Summer Meeting FEDSM2008, 2008, Paper No. 55103.

[22] B.M. Bossio, A.J. Blanco, F.H. Hernández, Eulerian-Eulerian modeling of non-Newtonian slurries flow in horizontal pipes, Proc. ASME 2009 Fluids Engineering Summer Meeting FEDSM2009, 2009, Paper No. 78019.

[23] K. Ekambara, R.S. Sanders, K. Nandakumar, J.H. Masliyah, Hydrodynamic simulation of horizontal slurry pipeline flow using ANSYS-CFX, Ind. Eng. Chem. Res. 48 (2009), 8159–8171.

[24] C.L. Antaya, K. Freeman, K. Adane, R.S. Sanders, Modelling concentrated slurry pipeline flows, Proc. ASME 2012 Fluids Engineering Summer Meeting FEDSM2012, 2012, Paper No. 72379.

[25] A. Hashemi, R.B. Spelay, K.F.K. Adane, R.S. Sanders, Solids velocity fluctuations in concentrated slurries, Can. J. Chem. Eng. 94 (2016) 1059–1065.

[26] D.R. Kaushal, T. Thinglas, Y. Tomita, S. Kuchii, H. Tsukamoto, CFD modeling for pipeline flow of fine particles at high concentration, Int. J. Multiphase Flow 43 (2012), 85-100.

[27] M.K. Gopaliya, D.R. Kaushal, Analysis of effect of grain size on various parameters of slurry flow through pipeline using CFD, Part. Sci. Technol. 33 (2015), 369–384.

[28] M.K. Gopaliya, D.R. Kaushal, Modeling of sand-water slurry flow through horizontal pipe using CFD, J. Hydrol. Hydromech. 64 (2016), 261–272.

[29] N. Kumar, M.K. Gopaliya, D.R. Kaushal, Experimental investigations and CFD modeling for flow of highly concentrated iron ore slurry through horizontal pipeline, Part. Sci. Technol. (2017), DOI: 10.1080/02726351.2017.1364313.

[30] M.K. Singh, S. Kumar, D. Ratha, Computational analysis on disposal of coal slurry at high solid concentrations through slurry pipeline, Int. J. Coal Prep. Util. (2017), DOI:

10.1080/19392699.2017.1346632.

[31] Y.Y. Jiang, P. Zhang, Numerical investigation of slush nitrogen flow in a horizontal pipe, Chem. Eng. Sci. 73 (2012), 169–180.

[32] Y.Y. Jiang, P. Zhang, Pressure drop and flow pattern of slush nitrogen in a horizontal pipe, AIChE J. 59 (2013), 1762–1773.

[33] M.C. Roco, N. Balakrishnam, Multi-dimensional flow analysis of liquid-solid mixtures, J. Rheol. 29 (1985), 431–456.

[34] R.C. Chen, Analysis of homogeneous slurry pipe flow, J. Mar. Sci. Technol. 2(1) (1994), 37–45.

[35] G.V. Messa, M. Malin, S. Malavasi, Numerical prediction of pressure gradient of slurry flows in horizontal pipes, Proc. ASME 2013 Pressure Vessels and Piping Conference PVP2013, 2013, Paper No. 97460.

[36] G.V. Messa, M. Malin, S. Malavasi, Numerical prediction of fully-suspended slurry flow in horizontal pipes, Powder Technol. 256 (2014), 61–70.

[37] G.V. Messa, S. Malavasi, Numerical prediction of particle distribution of solid-liquid slurries in straight pipes and bends, Eng. Appl. Comput. Fluid Mech. 8(3) (2014), 356–372.

[38] G.V. Messa, S. Malavasi, Improvements in the numerical prediction of fully-suspended slurry flow in horizontal pipes, Powder Technol. 270 (2015), 358–367.

[39] L. Chen, Y. Duan, W. Pu, C. Zhao, CFD simulation of coal-water slurry flowing in horizontal pipelines, Korean J. Chem. Eng. 26 (2009), 1144–1154.

[40] M.Z. Li, Y.P. He, Y.D. Liu, C. Huang, Hydrodynamic simulation of multi-sized high concentration slurry transport in pipelines, Ocean Eng. 163 (2018), 691–705.

[41] M.Z. Li, Y.P. He, Y.D. Liu, C. Huang, Effect of interaction of particles with different sizes on particle kinetics in multi-sized slurry transport by pipeline, Powder Technol. 338 (2018), 915–930.

[42] J. Ling, P.V. Skudarnov, C.X. Lin, M.A. Ebadian, Numerical investigations of liquid-solid slurry flows in a fully-developed turbulent flow region, Int. J. Heat Fluid Flow 24 (2003) 389–398.

[43] C.X. Lin, M.A. Ebadian, A numerical study of developing slurry flow in the entrance region of a horizontal pipe, Comput. Fluids 37 (2008) 965–974.

[44] R. Silva, P.M. Faia, F.A.P. Garcia, M.G. Rasteiro, Characterization of solid-liquid settling suspensions using Elecrtical Impedance Tomography: A comparison between numerical, experimental and visual information, Chem. Eng. Res. Des. 111 (2016), 223-242.

[45] J. Wang, T. Zhang, S. Wang, Heterogeneous ice slurry flow and concentration distribution in horizontal pipes, Int. J. Heat Mass Transfer 44 (2013), 425–434.

[46] R. Silva, F.A.P. Garcia, P. Faia, M.G. Rasteiro, Modeling solid-liquid homogeneous turbulent flow of neutrally buoyant particles using the mixture model: a study of length scales and closure coefficients, Multiphase Sci. Tech. 26 (2014), 199–227.

[47] D.B. Spalding, Numerical Computation of Multi-Phase Fluid Flow and Heat Transfer, in: C. Taylor, K. Morgan (Eds.), Prineridge Press Limited, Swansea, UK, 1980, pp. 139–168.

[48] N.S. Cheng, A.W.K. Law, Exponential formula for computing effective viscosity, Powder Technol. 129 (1–3) (2003), 150–160.

[49] L. Schiller, A. Naumann, A drag coefficient correlation, Z. Ver. Dtsch. Ing. 77 (1935) 318320.

[50] G.V. Messa, Two–fluid model for solid–liquid flows in pipeline systems, PhD Thesis, Politecnico di Milano, 2013.

[51] M. Ishii, K. Mishima, Two-fluid model and hydrodynamic constitutive relations, Nucl. Eng. Des. 82 (1984) 107–126.

[52] A. Haider, O. Levenspiel, Drag coefficient and terminal velocity of spherical and non-spherical particles, Powder Technol. 58 (1989) 63–70.

[53] B.E. Launder, D.B. Spalding, The numerical computation of turbulent flows, Comput. Meth. Appl. Mech. Eng. 3 (1974) 269289.

[54] D.B. Spalding, A novel finite-difference formulation for differential expressions involving both first and second derivatives, Int. J. Numer. Methods Eng. 4(4) (1972) 551–559.

[55] D.B. Spalding, Mathematical modelling of fluid-mechanics, heat-transfer and chemical-reaction processes: a lecture course, CFDU Report HTS/80/1, Imperial College, London, 1980.

[56] V. Matoušek, J. Krupi č ka, J. Konfršt, V. P ě ník, Internal structure of settling-slurry flows: solids distribution and friction in horizontal pipe, Proc. 16 th Int. Conf. Transport and Sedimentation of Solid Particles, 2013.

[57] V. Matoušek, Pressure drop and flow patterns in sand-mixture pipes, Exp. Therm. Fluid

Sci. 26 (2002) 693–702.

[58] R.G. Gillies, C.A. Shook, J. Xu, Modelling heterogeneous slurry flow at high velocities, Can. J. Chem. Eng. 82 (2004) 1060–1065.

[59] R.G. Gillies, Pipeline flow of coarse particle slurries, PhD Thesis, University of Saskatchewan, Saskatoon, Canada, 1993.

[60] E.J. Wasp, J.P. Kenny, R.L. Gandhi, Solid-liquid flow: slurry pipeline transportation. Gulf Publishing, Houston, Texas, 1979.

[61] N.P. Brown, N.I. Heywood, Slurry handling: design of solid-liquid systems. Elsevier Science Publishing, New York, 1991.

[62] R. Clift, J.R. Grace, M.E. Weber, Bubbles, drops and particles. Academic Press, 1978.

[63] R. Turton, O. Levenspiel, A short note on the drag correlation for spheres, Powder Technol. 47 (1986) 83–86.

[64] M.C. Roco, C.A. Shook, Modeling of slurry flow: the effect of particle size, Can. J. Chem. Eng. 61 (1983), 494–503.

[65] O.A. El Masry, M.M. El Halawany, Velocity and concentration distribution in slurry pipe flow, WIT Transactions on Modelling and Simulation 4 (1992), 18 pages.

[66] R. Mishra, S.N. Singh, V. Seshadri, Velocity measurement in solid-liquid flows using an impact probe, Flow. Meas. Instrum. 8 (1997), 157–165.

[67] A. Hashemi, A. Sadighian, S.I.A., R.S. Sanders, Solid velocity and concentration fluctuations in highly concentrated liquid-solid (slurry) pipe flows, Int. J. Multiphase Flow 66 (2014) 46–61.

Graphical abstract

Highlights

- Convergence and sensitivity assessment followed by calibration and validation
- Critical inspection of diffcult-to-measure parameters
- Investigation of pipe size-up scalability of a two-fluid model
- Precise specification of the application domain
- Development of best practice guidelines for slurry pipe flow simulation

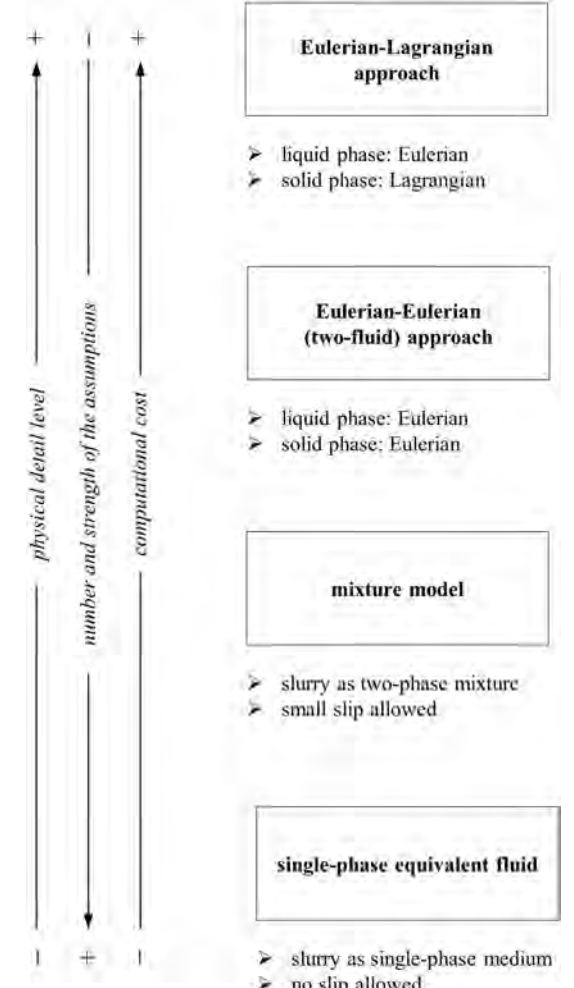
+
|
+
physical detail level
number and strength of the assumptions
computational cost
|
+
|
Eulerian-Lagrangian approach
liquid phase: Eulerian
solid phase: Lagrangian
Eulerian-Eulerian (two-fluid) approach
liquid phase: Eulerian
solid phase: Eulerian
mixture model
slurry as two-phase mixture
small slip allowed
single-phase equivalent fluid
slurry as single-phase medium
no slip allowed

Figure 1

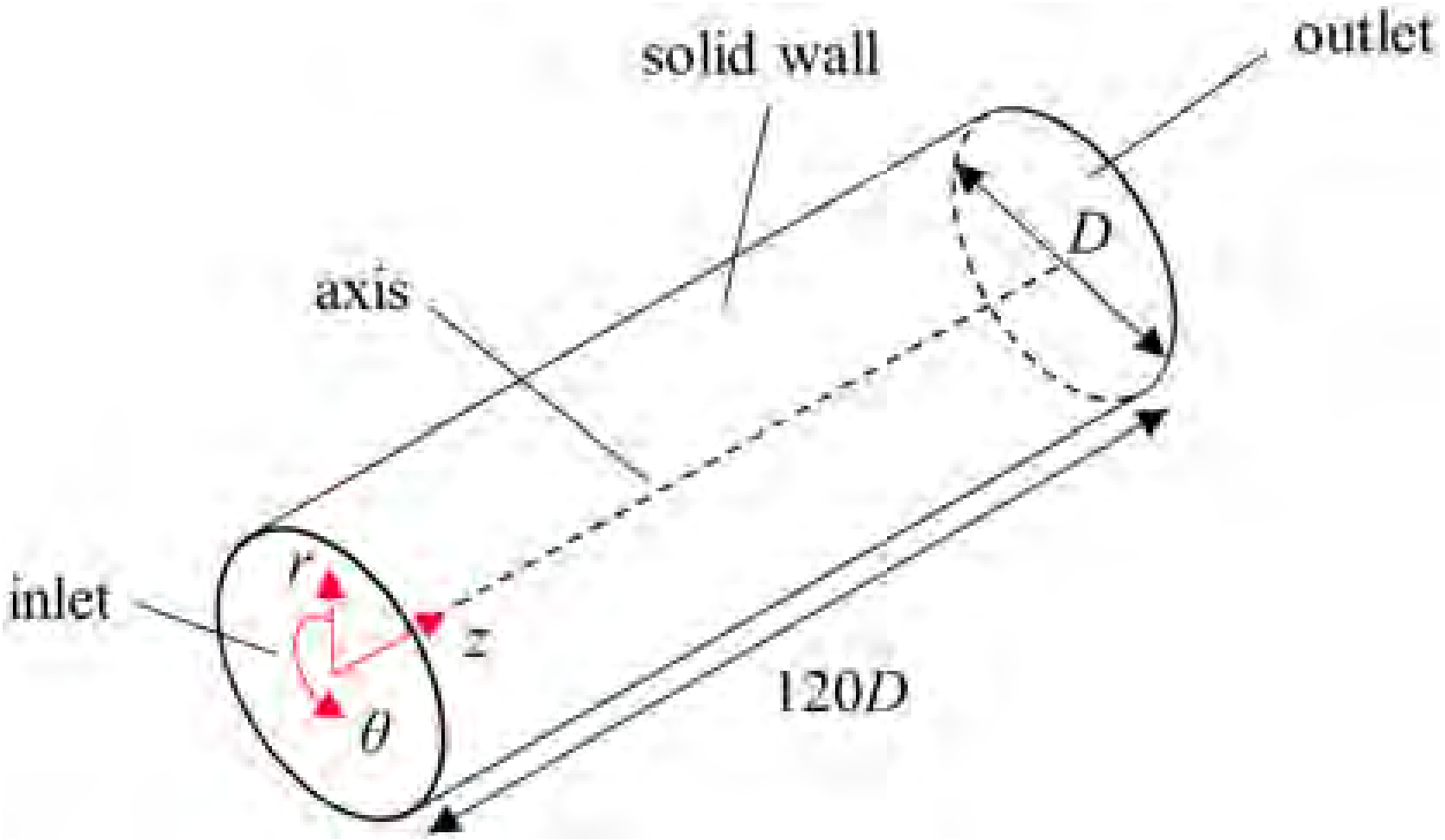

Figure 2

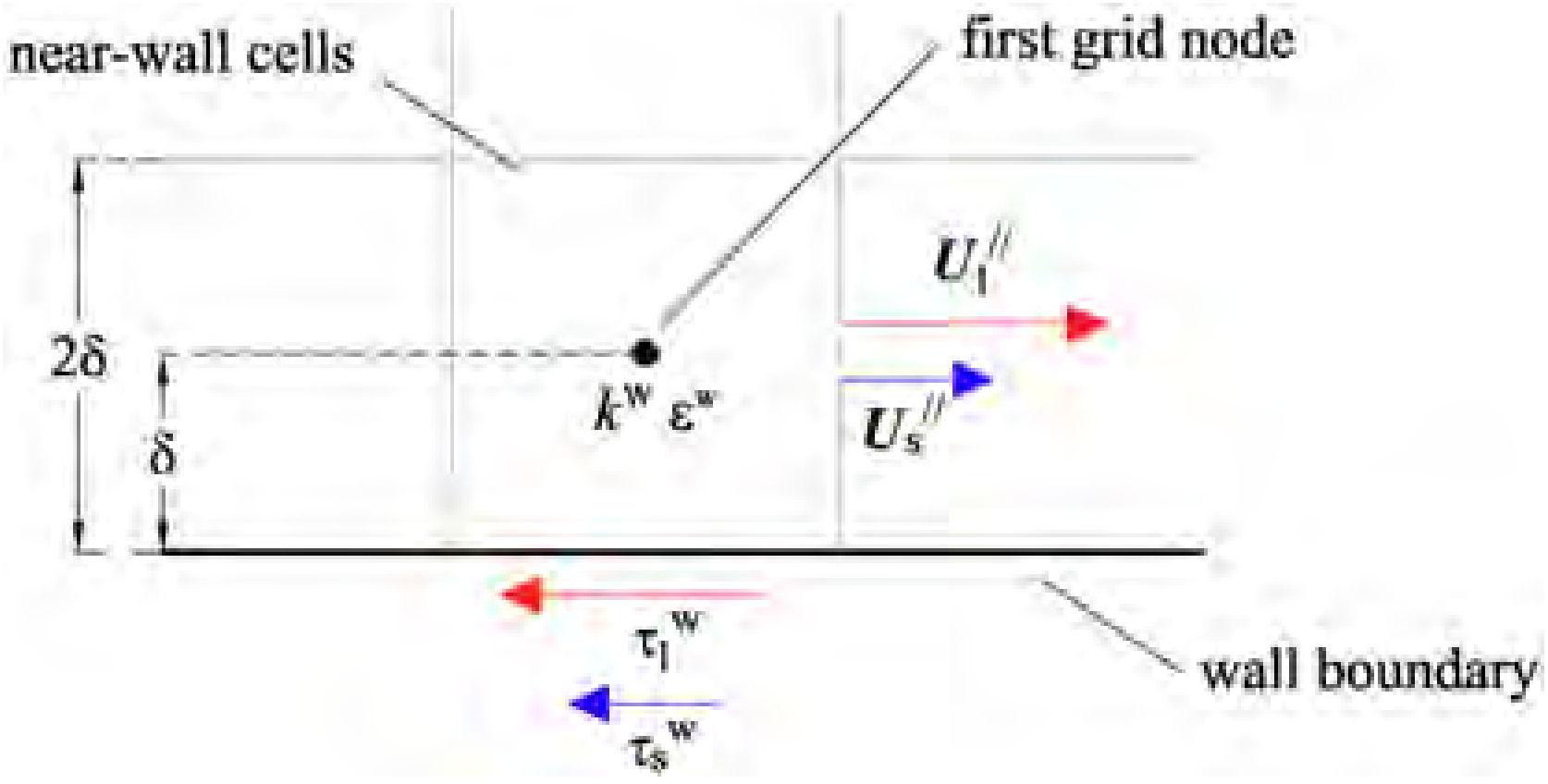
near-wall cells
first grid node
U_l''
2δ
k^w ε^w
U_s''
δ
τ_l^w
wall boundary
τ_s^w

Figure 3

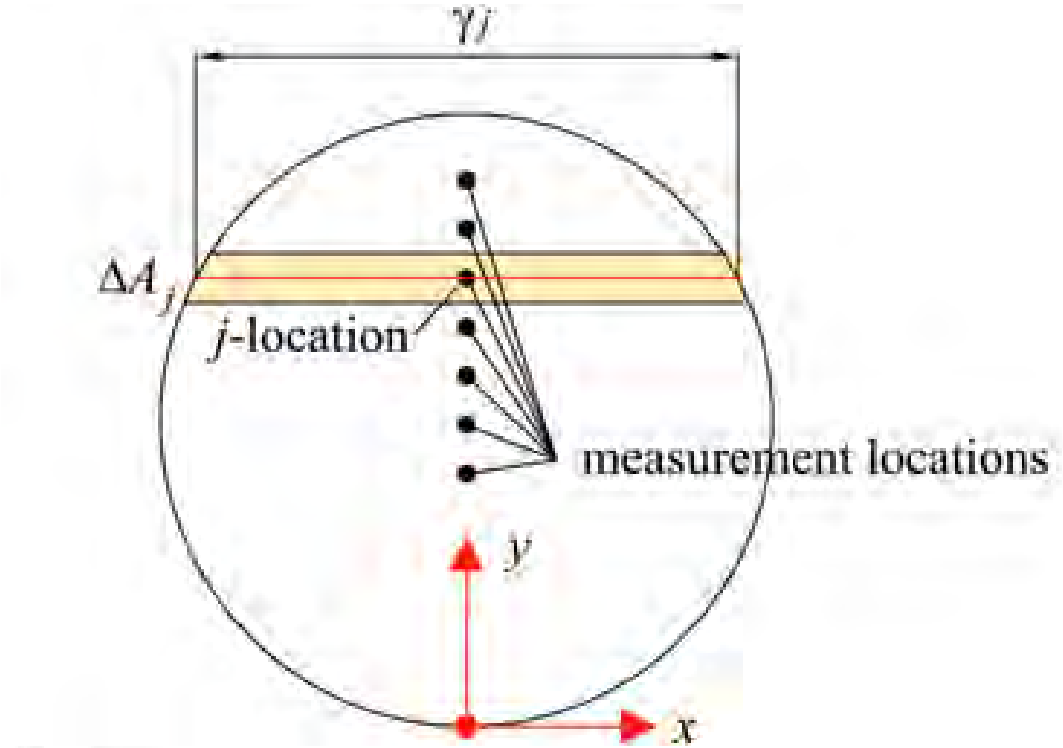
γj
ΔAj
j-location
measurement locations
y
x

(a)

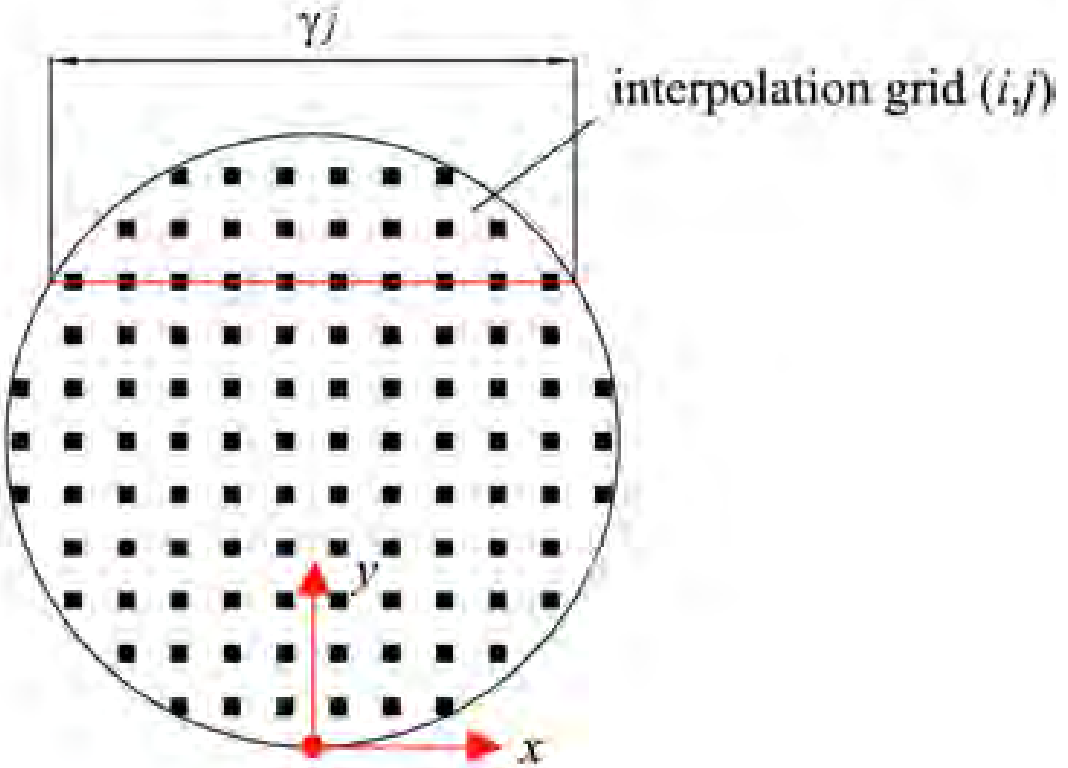
γj
interpolation grid (i,j)
y
x

(b)

Figure 4

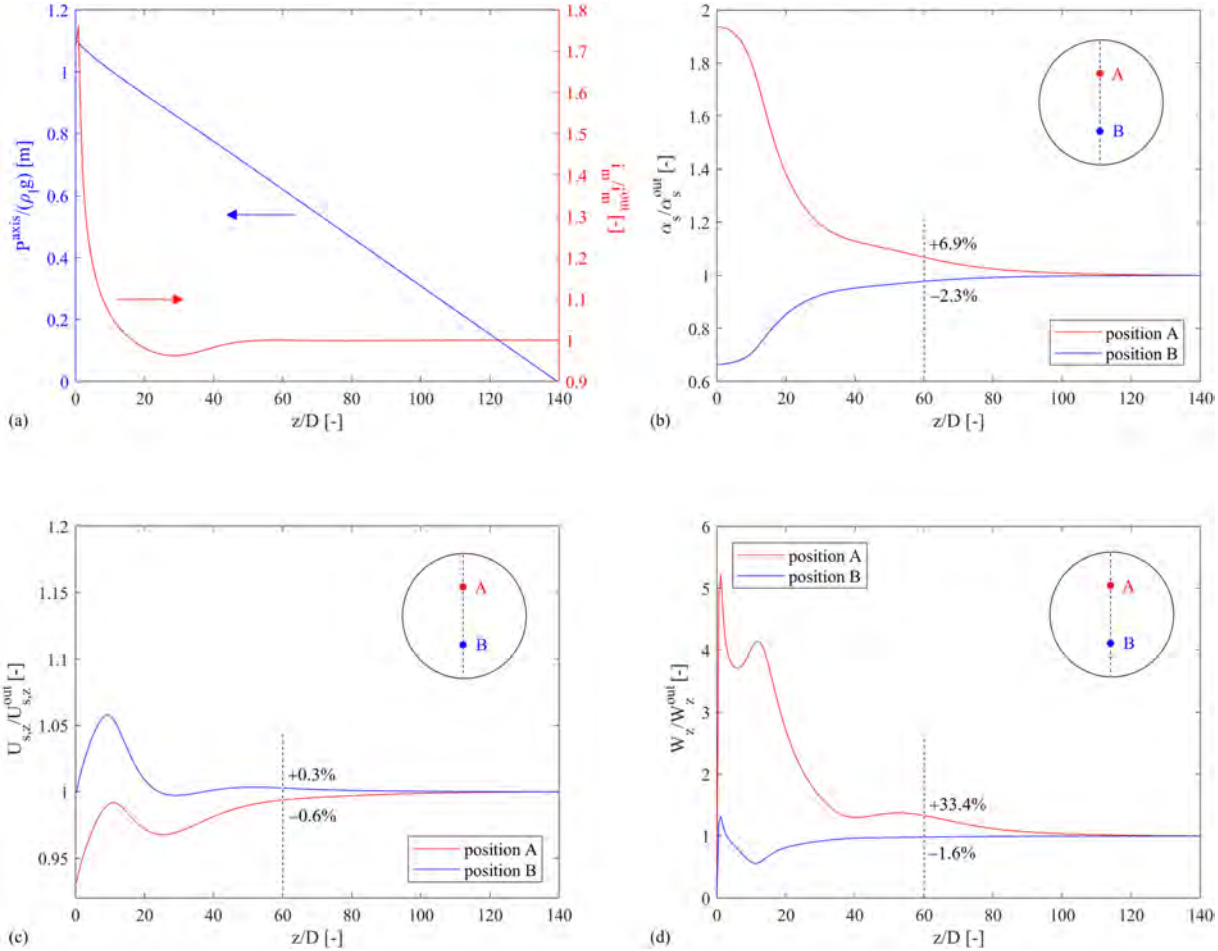
(a)
$p^{axis}/(\rho_l g)$ [m]
$\dot{m}/\dot{m}^{out}$ [-]
z/D [-]
(b)
α_s/α_s^{out} [-]
+6.9%
−2.3%
position A
position B
A
B
z/D [-]
(c)
$U_{s,Z}/U_{s,Z}^{out}$ [-]
+0.3%
−0.6%
position A
position B
A
B
z/D [-]
(d)
W_z/W_z^{out} [-]
position A
position B
+33.4%
−1.6%
A
B
z/D [-]

Figure 5

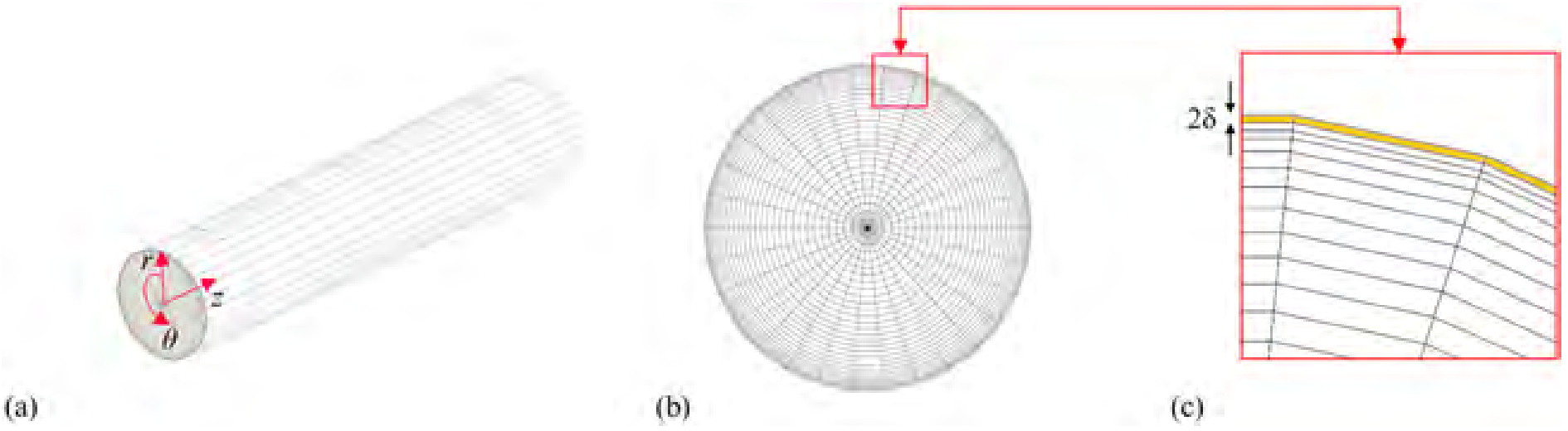

Figure 6

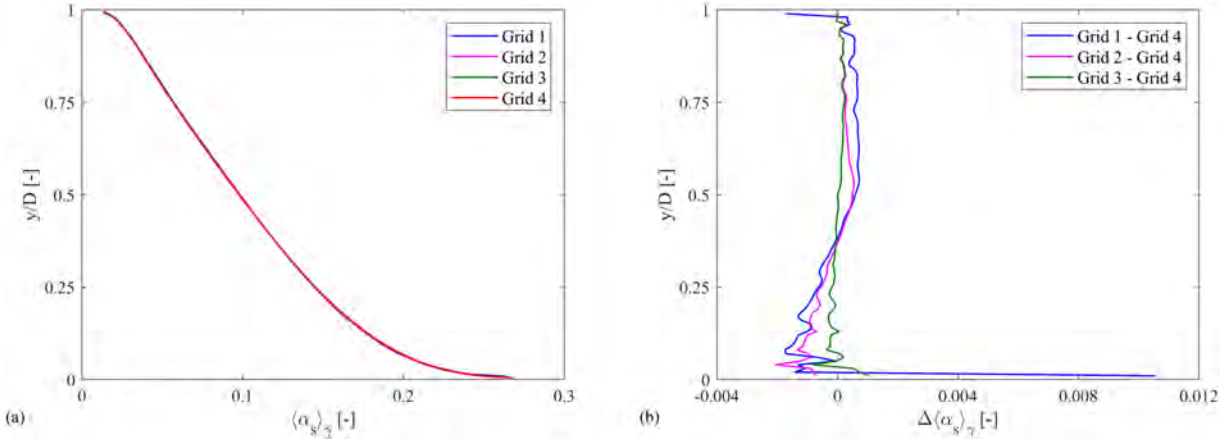
Grid 1
Grid 2
Grid 3
Grid 4
y/D [-]
1
0.75
0.5
0.25
0
0
0.1
0.2
0.3
(a)
$\langle \alpha_g \rangle_{\bar{\gamma}}$ [-]
Grid 1 - Grid 4
Grid 2 - Grid 4
Grid 3 - Grid 4
y/D [-]
1
0.75
0.5
0.25
0
-0.004
0
0.004
0.008
0.012
(b)
$\Delta\langle \alpha_g \rangle_{\gamma}$ [-]

Figure 7

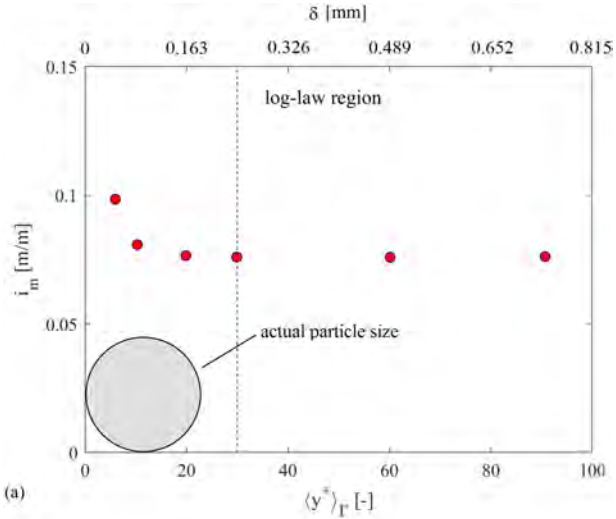
δ [mm]
0
0.163
0.326
0.489
0.652
0.815
log-law region
actual particle size
i_m [m/m]
0.15
0.1
0.05
0
0
20
40
60
80
100
$\langle y^+ \rangle_\Gamma$ [-]
(a)

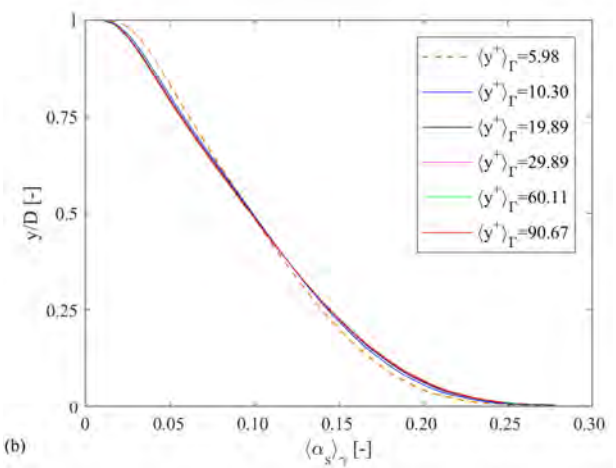
$\langle y^+ \rangle_\Gamma$=5.98
$\langle y^+ \rangle_\Gamma$=10.30
$\langle y^+ \rangle_\Gamma$=19.89
$\langle y^+ \rangle_\Gamma$=29.89
$\langle y^+ \rangle_\Gamma$=60.11
$\langle y^+ \rangle_\Gamma$=90.67
y/D [-]
1
0.75
0.5
0.25
0
0
0.05
0.10
0.15
0.20
0.25
0.30
$\langle \alpha_s \rangle_\gamma$ [-]
(b)

Figure 8

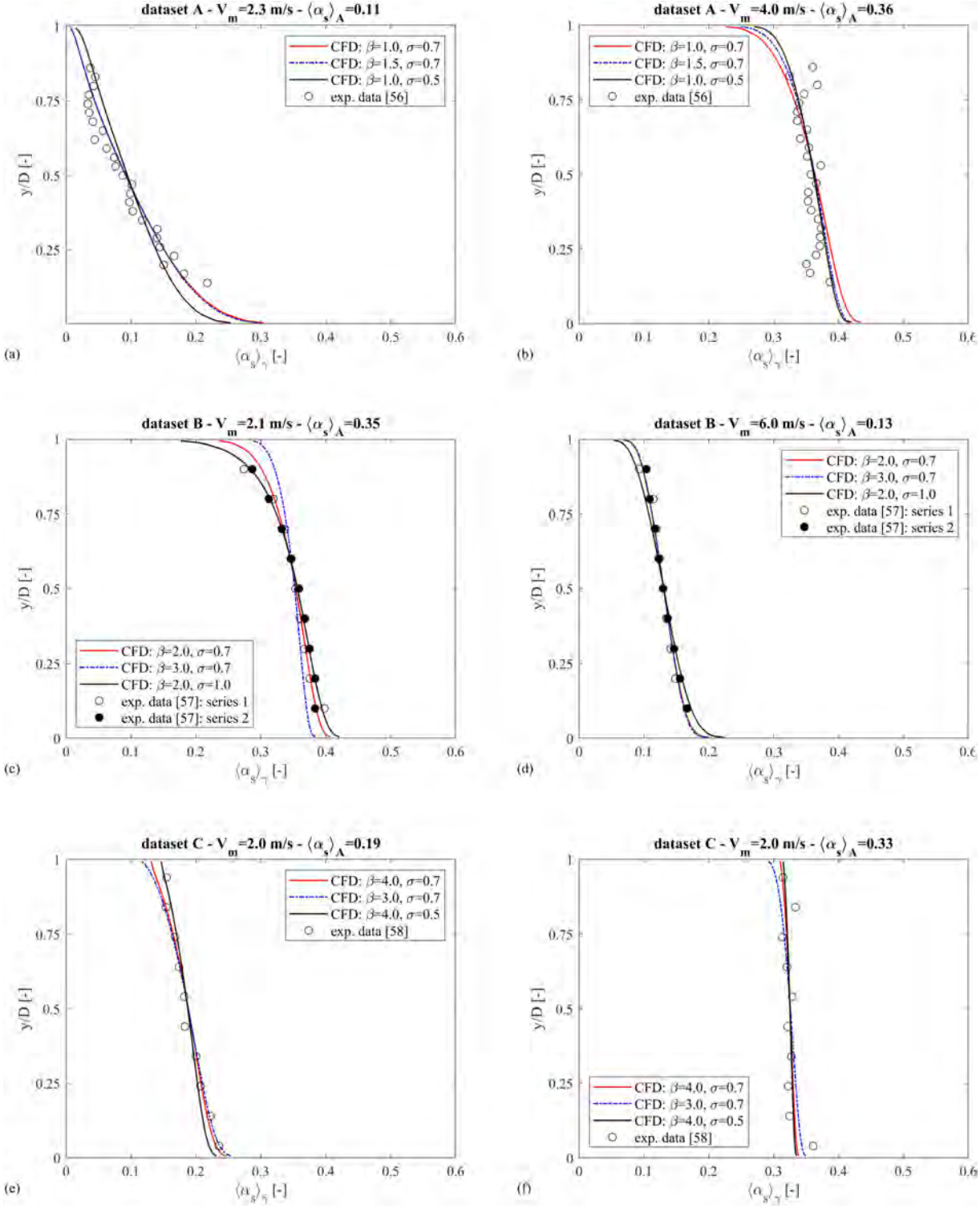
dataset A - V_m=2.3 m/s - $\langle\alpha_s\rangle_A$=0.11
CFD: β=1.0, σ=0.7
CFD: β=1.5, σ=0.7
CFD: β=1.0, σ=0.5
exp. data [56]
y/D [-]
$\langle\alpha_s\rangle_\gamma$ [-]
(a)
dataset A - V_m=4.0 m/s - $\langle\alpha_s\rangle_A$=0.36
CFD: β=1.0, σ=0.7
CFD: β=1.5, σ=0.7
CFD: β=1.0, σ=0.5
exp. data [56]
y/D [-]
$\langle\alpha_s\rangle_\gamma$ [-]
(b)
dataset B - V_m=2.1 m/s - $\langle\alpha_s\rangle_A$=0.35
CFD: β=2.0, σ=0.7
CFD: β=3.0, σ=0.7
CFD: β=2.0, σ=1.0
exp. data [57]: series 1
exp. data [57]: series 2
y/D [-]
$\langle\alpha_s\rangle_\gamma$ [-]
(c)
dataset B - V_m=6.0 m/s - $\langle\alpha_s\rangle_A$=0.13
CFD: β=2.0, σ=0.7
CFD: β=3.0, σ=0.7
CFD: β=2.0, σ=1.0
exp. data [57]: series 1
exp. data [57]: series 2
y/D [-]
$\langle\alpha_s\rangle_\gamma$ [-]
(d)
dataset C - V_m=2.0 m/s - $\langle\alpha_s\rangle_A$=0.19
CFD: β=4.0, σ=0.7
CFD: β=3.0, σ=0.7
CFD: β=4.0, σ=0.5
exp. data [58]
y/D [-]
$\langle\alpha_s\rangle_\gamma$ [-]
(e)
dataset C - V_m=2.0 m/s - $\langle\alpha_s\rangle_A$=0.33
CFD: β=4.0, σ=0.7
CFD: β=3.0, σ=0.7
CFD: β=4.0, σ=0.5
exp. data [58]
y/D [-]
$\langle\alpha_s\rangle_\gamma$ [-]
(f)

Figure 9

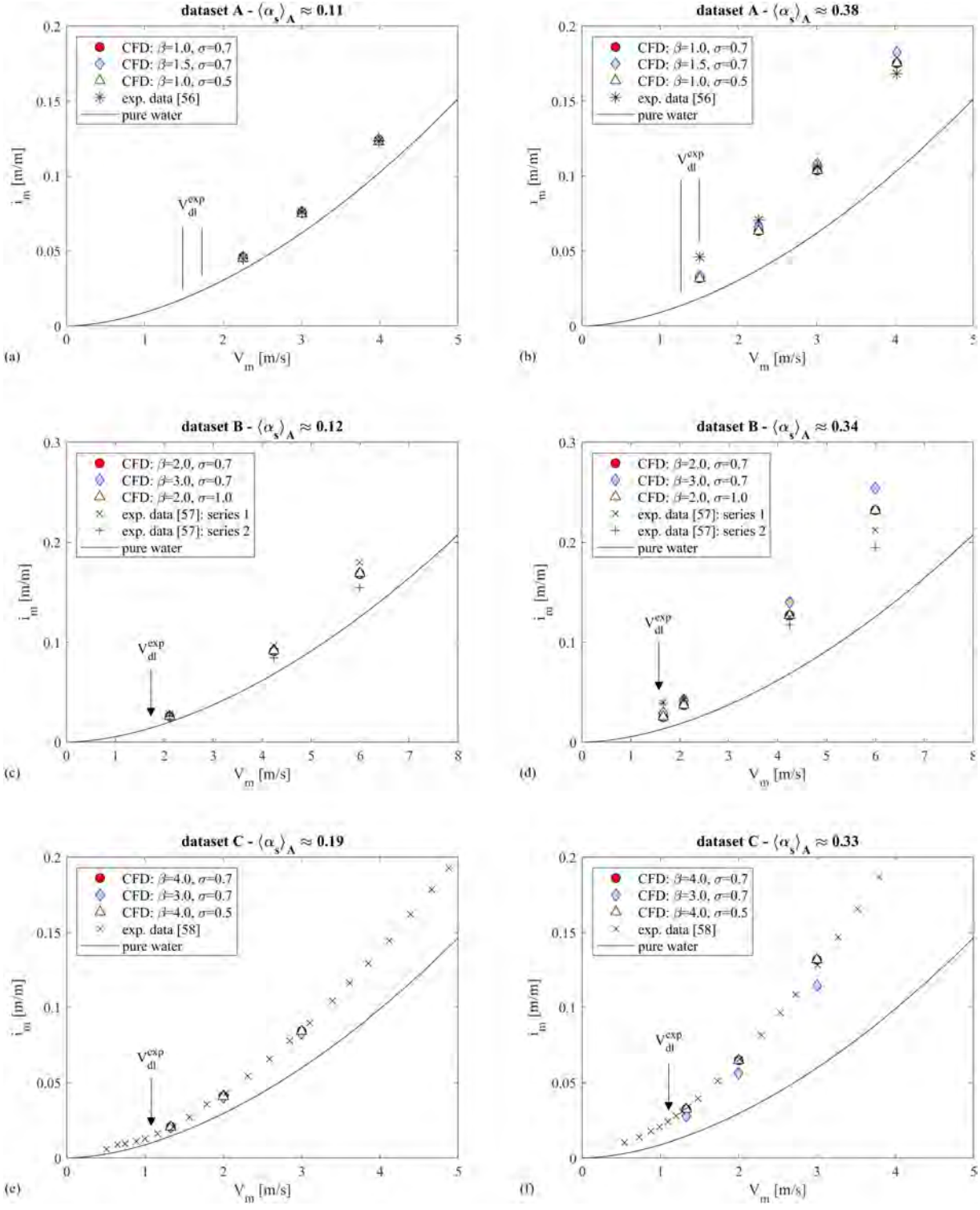
dataset A - $\langle\alpha_s\rangle_A \approx 0.11$
CFD: β=1.0, σ=0.7
CFD: β=1.5, σ=0.7
CFD: β=1.0, σ=0.5
exp. data [56]
pure water
V_{dl}^{exp}
i_m [m/m]
V_m [m/s]
(a)
dataset A - $\langle\alpha_s\rangle_A \approx 0.38$
CFD: β=1.0, σ=0.7
CFD: β=1.5, σ=0.7
CFD: β=1.0, σ=0.5
exp. data [56]
pure water
V_{dl}^{exp}
i_m [m/m]
V_m [m/s]
(b)
dataset B - $\langle\alpha_s\rangle_A \approx 0.12$
CFD: β=2.0, σ=0.7
CFD: β=3.0, σ=0.7
CFD: β=2.0, σ=1.0
exp. data [57]: series 1
exp. data [57]: series 2
pure water
V_{dl}^{exp}
i_m [m/m]
V_m [m/s]
(c)
dataset B - $\langle\alpha_s\rangle_A \approx 0.34$
CFD: β=2.0, σ=0.7
CFD: β=3.0, σ=0.7
CFD: β=2.0, σ=1.0
exp. data [57]: series 1
exp. data [57]: series 2
pure water
V_{dl}^{exp}
i_m [m/m]
V_m [m/s]
(d)
dataset C - $\langle\alpha_s\rangle_A \approx 0.19$
CFD: β=4.0, σ=0.7
CFD: β=3.0, σ=0.7
CFD: β=4.0, σ=0.5
exp. data [58]
pure water
V_{dl}^{exp}
i_m [m/m]
V_m [m/s]
(e)
dataset C - $\langle\alpha_s\rangle_A \approx 0.33$
CFD: β=4.0, σ=0.7
CFD: β=3.0, σ=0.7
CFD: β=4.0, σ=0.5
exp. data [58]
pure water
V_{dl}^{exp}
i_m [m/m]
V_m [m/s]
(f)

Figure 10

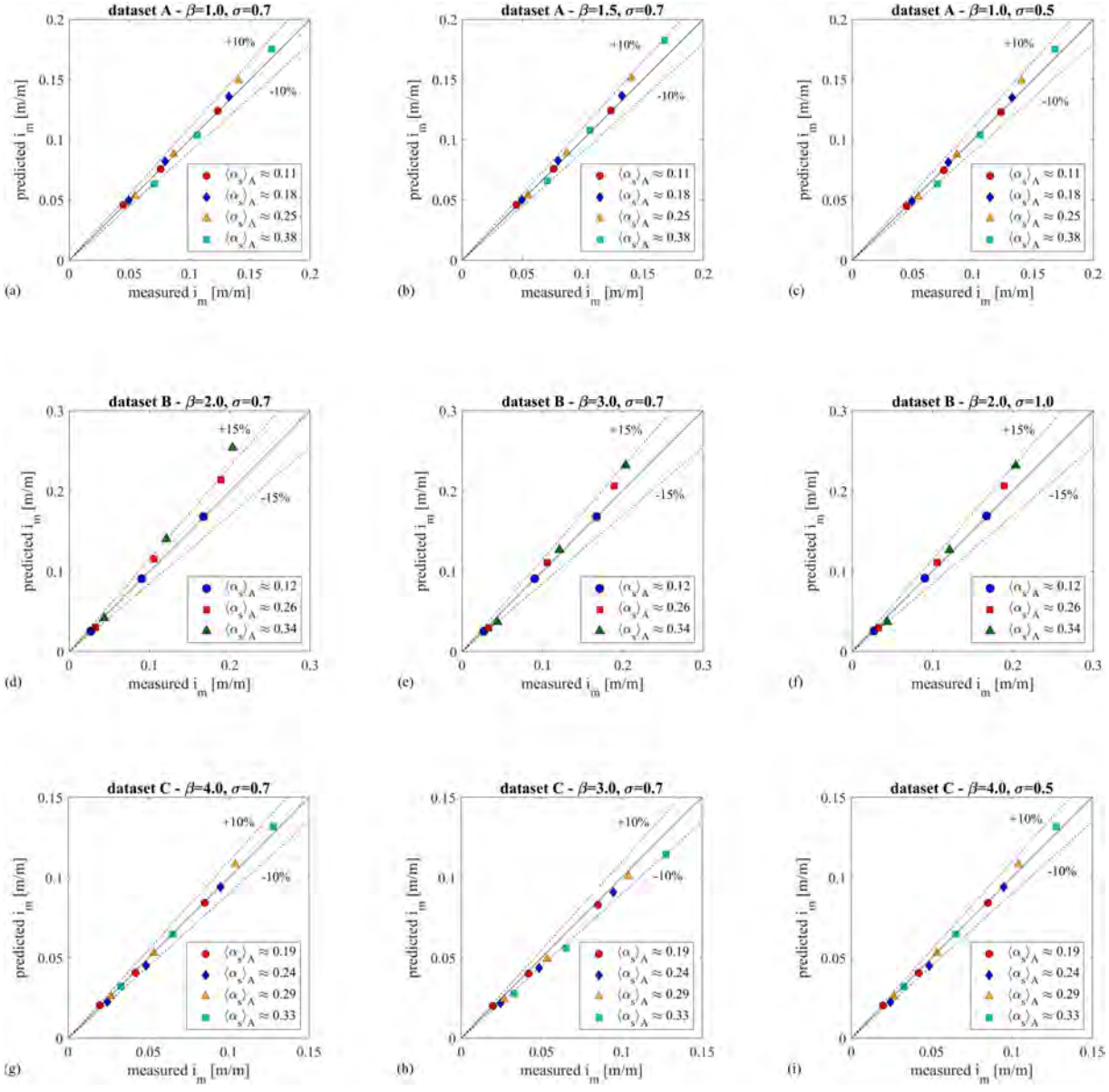
dataset A - β=1.0, σ=0.7
dataset A - β=1.5, σ=0.7
dataset A - β=1.0, σ=0.5
dataset B - β=2.0, σ=0.7
dataset B - β=3.0, σ=0.7
dataset B - β=2.0, σ=1.0
dataset C - β=4.0, σ=0.7
dataset C - β=3.0, σ=0.7
dataset C - β=4.0, σ=0.5
+10%
-10%
+15%
-15%
predicted i_m [m/m]
measured i_m [m/m]
⟨α_s⟩_A ≈ 0.11
⟨α_s⟩_A ≈ 0.18
⟨α_s⟩_A ≈ 0.25
⟨α_s⟩_A ≈ 0.38
⟨α_s⟩_A ≈ 0.12
⟨α_s⟩_A ≈ 0.26
⟨α_s⟩_A ≈ 0.34
⟨α_s⟩_A ≈ 0.19
⟨α_s⟩_A ≈ 0.24
⟨α_s⟩_A ≈ 0.29
⟨α_s⟩_A ≈ 0.33
(a)
(b)
(c)
(d)
(e)
(f)
(g)
(b)
(i)

Figure 11

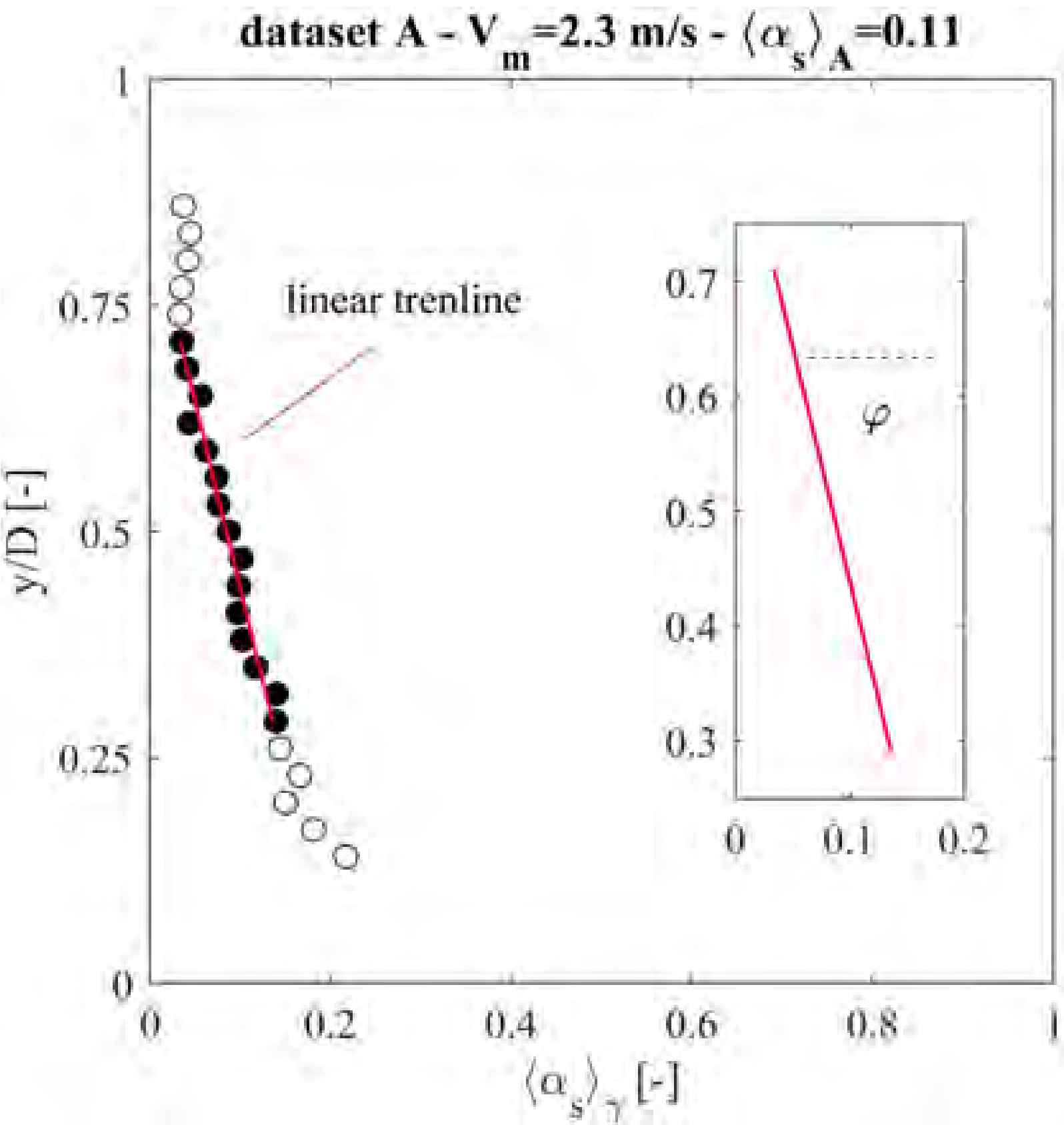
dataset A - V_m=2.3 m/s - ⟨α_s⟩_A=0.11
linear trenline
y/D [-]
⟨α_s⟩_γ [-]
φ
0
0.25
0.5
0.75
1
0.2
0.4
0.6
0.8
0.3
0.7
0.1

Figure 12

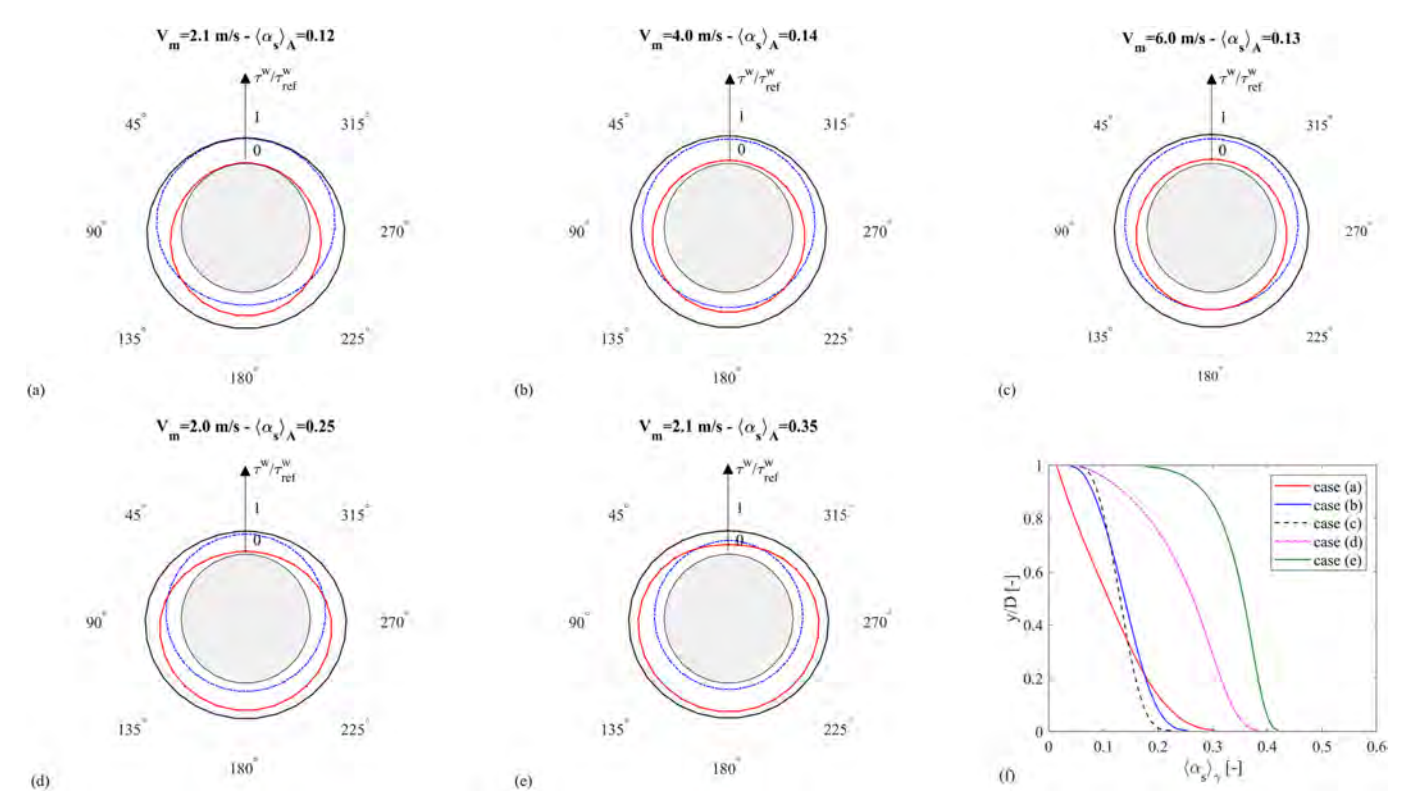
V_m=2.1 m/s - ⟨α_s⟩_A=0.12
V_m=4.0 m/s - ⟨α_s⟩_A=0.14
V_m=6.0 m/s - ⟨α_s⟩_A=0.13
V_m=2.0 m/s - ⟨α_s⟩_A=0.25
V_m=2.1 m/s - ⟨α_s⟩_A=0.35
τ^w/τ^w_ref
1
0
45°
315°
90°
270°
135°
225°
180°
(a)
(b)
(c)
(d)
(e)
(f)
case (a)
case (b)
case (c)
case (d)
case (e)
y/D [-]
⟨α_s⟩_γ [-]
0
0.1
0.2
0.3
0.4
0.5
0.6
0.8
1

Figure 13

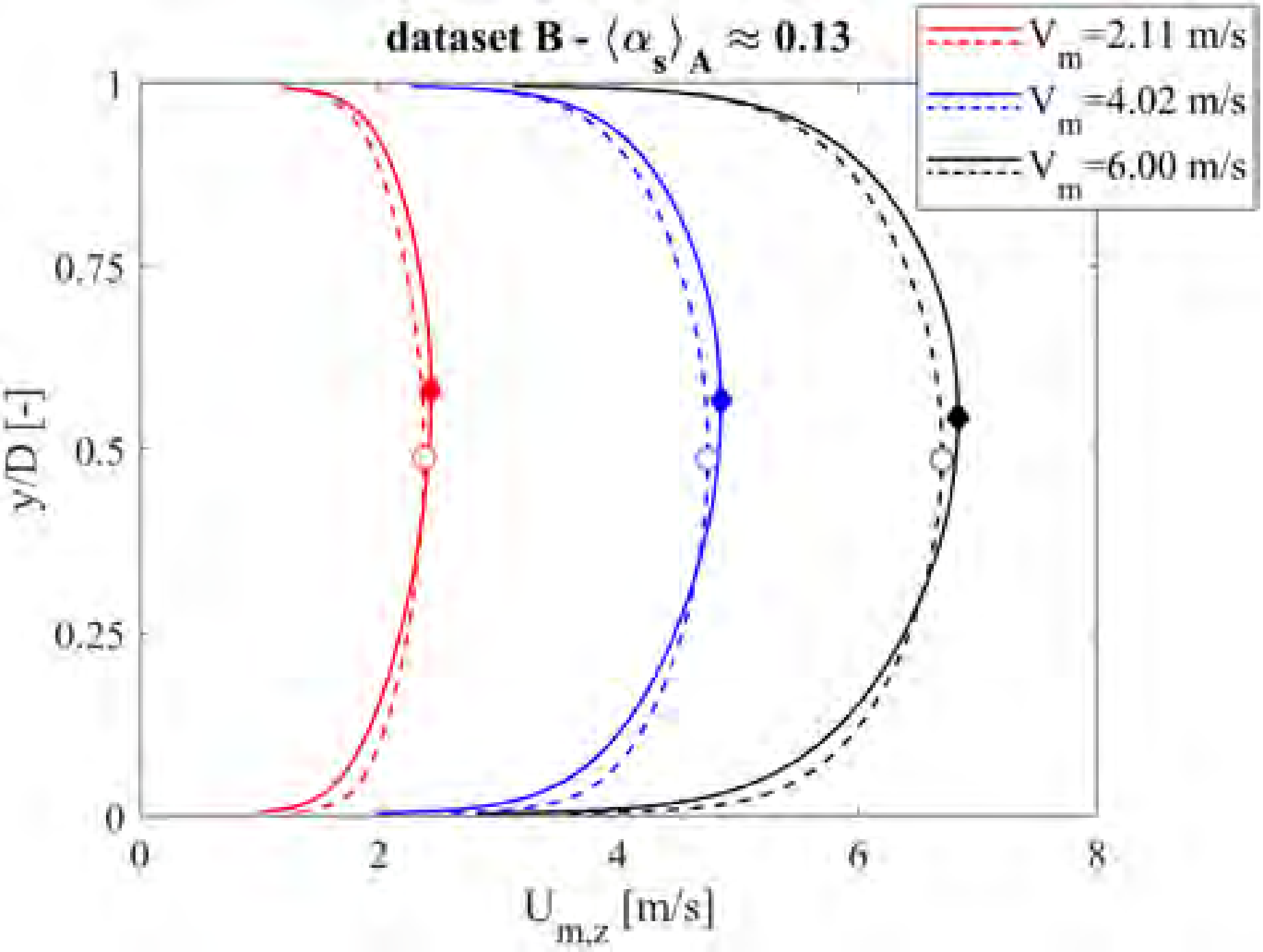
dataset B - $\langle \alpha_s \rangle_A \approx 0.13$
V_m=2.11 m/s
V_m=4.02 m/s
V_m=6.00 m/s
y/D [-]
0
0.25
0.5
0.75
1
0
2
4
6
8
$U_{m,z}$ [m/s]

Figure 14

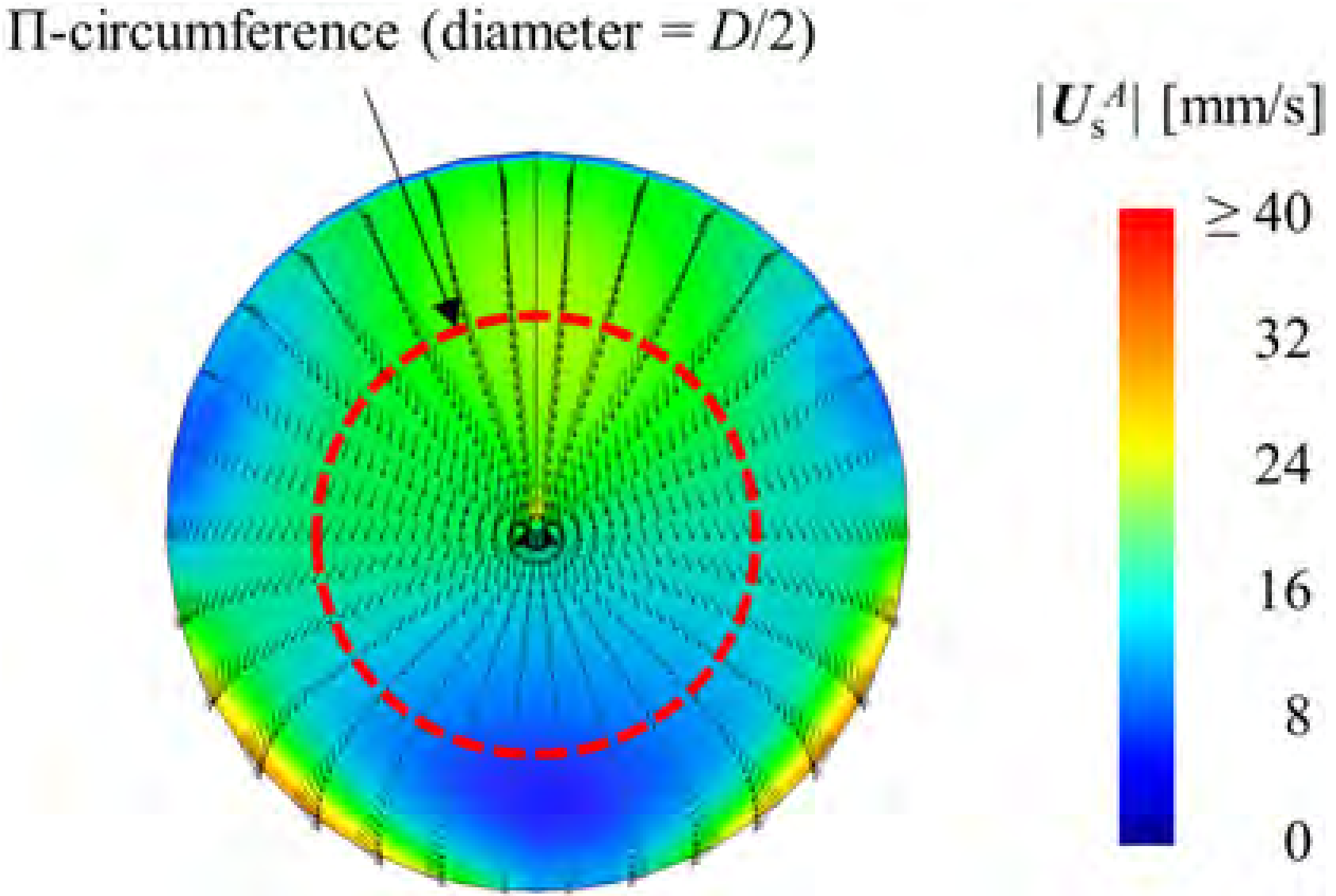

Figure 15

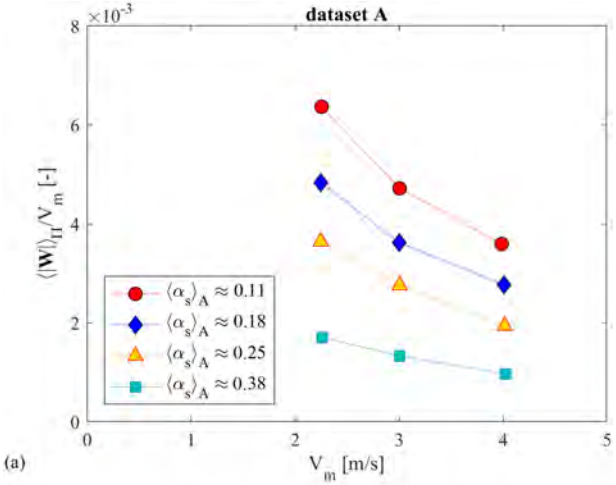
dataset A
×10^-3
⟨|W|⟩_Π/V_m [-]
V_m [m/s]
⟨α_s⟩_A ≈ 0.11
⟨α_s⟩_A ≈ 0.18
⟨α_s⟩_A ≈ 0.25
⟨α_s⟩_A ≈ 0.38
(a)

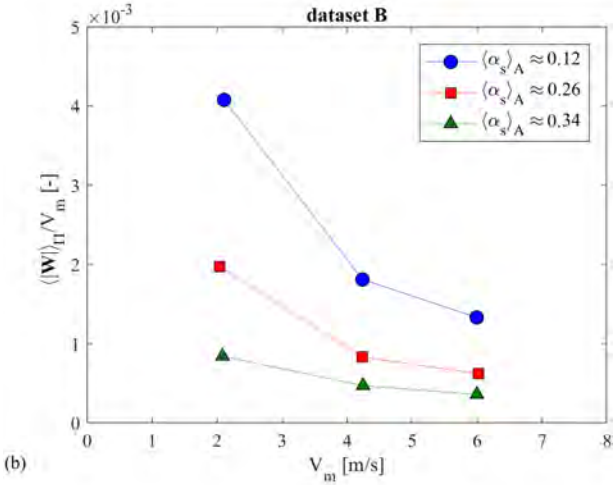
dataset B
×10^-3
⟨|W|⟩_Π/V_m [-]
V_m [m/s]
⟨α_s⟩_A ≈ 0.12
⟨α_s⟩_A ≈ 0.26
⟨α_s⟩_A ≈ 0.34
(b)

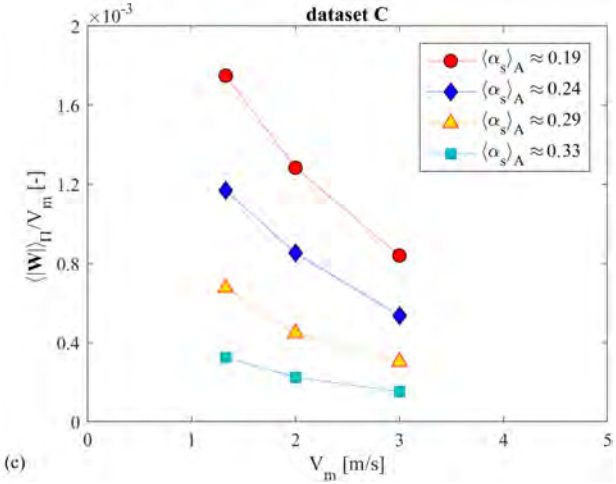
dataset C
×10^-3
⟨|W|⟩_Π/V_m [-]
V_m [m/s]
⟨α_s⟩_A ≈ 0.19
⟨α_s⟩_A ≈ 0.24
⟨α_s⟩_A ≈ 0.29
⟨α_s⟩_A ≈ 0.33
(c)

Figure 16

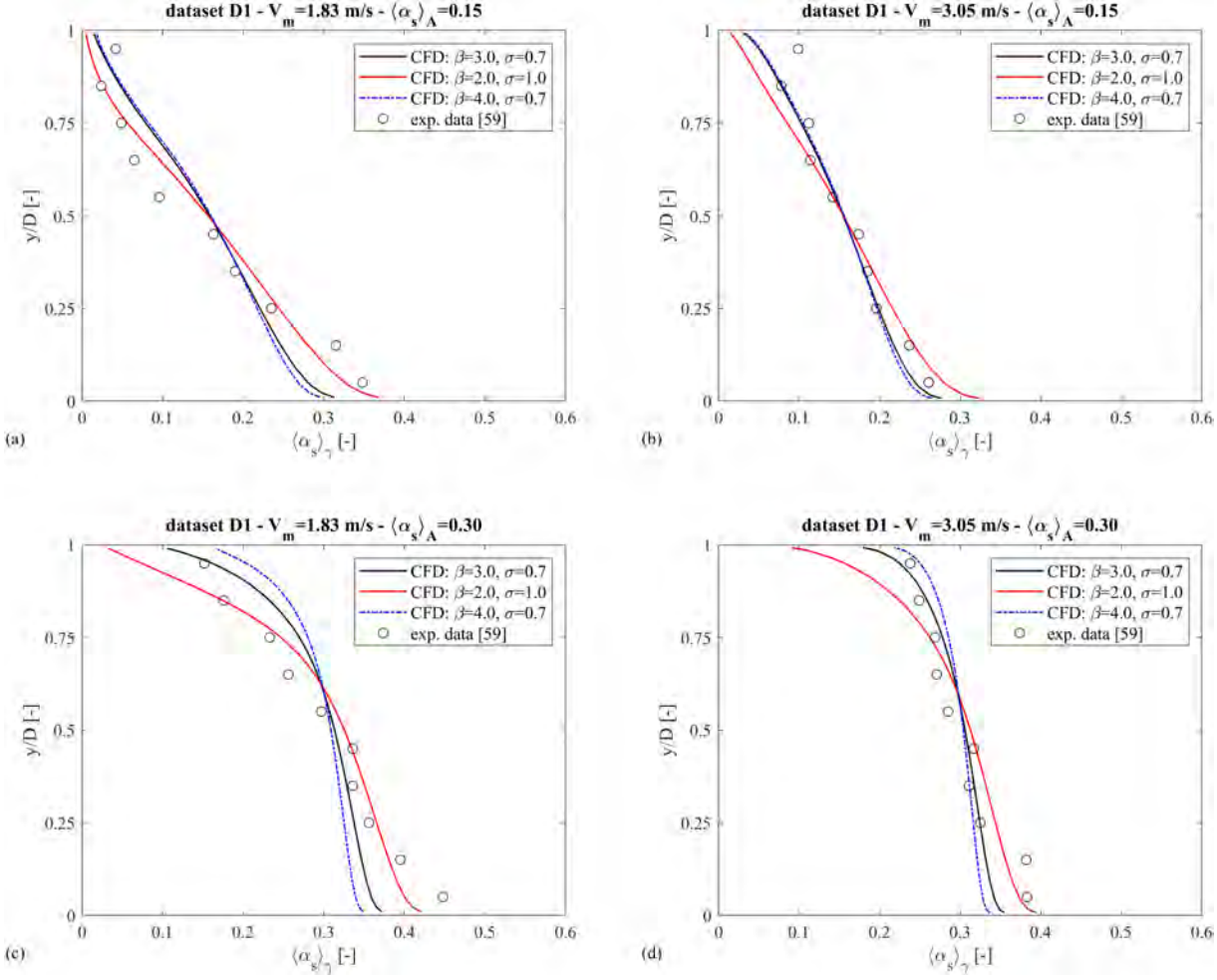
dataset D1 - V_m=1.83 m/s - $\langle\alpha_s\rangle_A$=0.15
CFD: β=3.0, σ=0.7
CFD: β=2.0, σ=1.0
CFD: β=4.0, σ=0.7
exp. data [59]
y/D [-]
$\langle\alpha_s\rangle_\gamma$ [-]
(a)
dataset D1 - V_m=3.05 m/s - $\langle\alpha_s\rangle_A$=0.15
CFD: β=3.0, σ=0.7
CFD: β=2.0, σ=1.0
CFD: β=4.0, σ=0.7
exp. data [59]
y/D [-]
$\langle\alpha_s\rangle_\gamma$ [-]
(b)
dataset D1 - V_m=1.83 m/s - $\langle\alpha_s\rangle_A$=0.30
CFD: β=3.0, σ=0.7
CFD: β=2.0, σ=1.0
CFD: β=4.0, σ=0.7
exp. data [59]
y/D [-]
$\langle\alpha_s\rangle_\gamma$ [-]
(c)
dataset D1 - V_m=3.05 m/s - $\langle\alpha_s\rangle_A$=0.30
CFD: β=3.0, σ=0.7
CFD: β=2.0, σ=1.0
CFD: β=4.0, σ=0.7
exp. data [59]
y/D [-]
$\langle\alpha_s\rangle_\gamma$ [-]
(d)

Figure 17

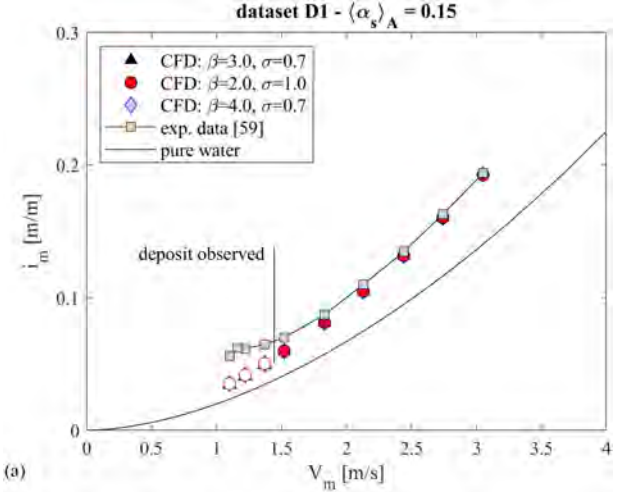
dataset D1 - $\langle \alpha_s \rangle_A$ = 0.15
CFD: β=3.0, σ=0.7
CFD: β=2.0, σ=1.0
CFD: β=4.0, σ=0.7
exp. data [59]
pure water
deposit observed
i_m [m/m]
V_m [m/s]
(a)

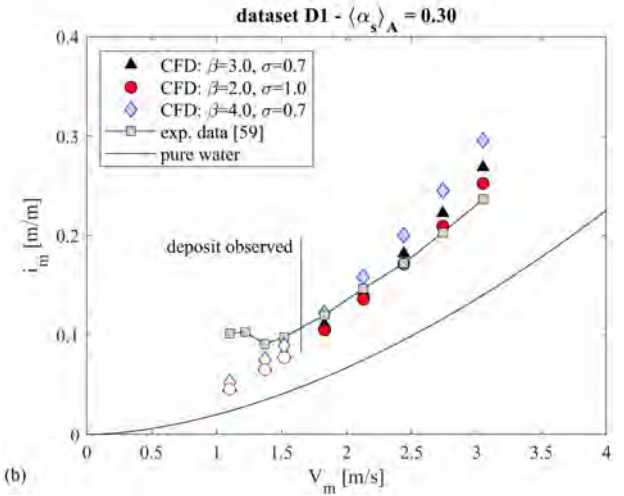
dataset D1 - $\langle \alpha_s \rangle_A$ = 0.30
CFD: β=3.0, σ=0.7
CFD: β=2.0, σ=1.0
CFD: β=4.0, σ=0.7
exp. data [59]
pure water
deposit observed
i_m [m/m]
V_m [m/s]
(b)

Figure 18

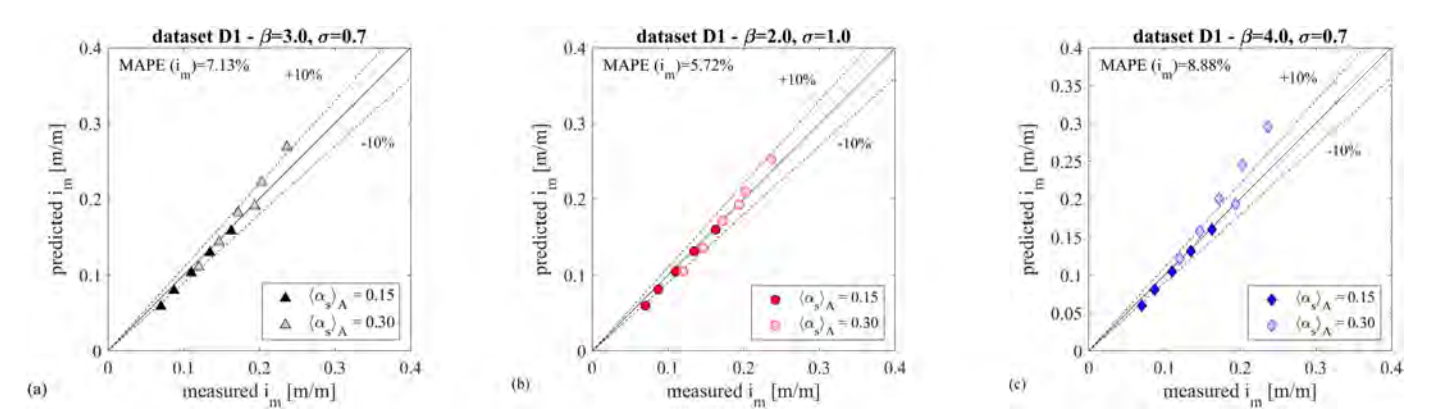
dataset D1 - β=3.0, σ=0.7
MAPE (i_m)=7.13%
+10%
-10%
⟨α_s⟩_A = 0.15
⟨α_s⟩_A = 0.30
predicted i_m [m/m]
measured i_m [m/m]
(a)
dataset D1 - β=2.0, σ=1.0
MAPE (i_m)=5.72%
+10%
-10%
⟨α_s⟩_A = 0.15
⟨α_s⟩_A = 0.30
predicted i_m [m/m]
measured i_m [m/m]
(b)
dataset D1 - β=4.0, σ=0.7
MAPE (i_m)=8.88%
+10%
-10%
⟨α_s⟩_A = 0.15
⟨α_s⟩_A = 0.30
predicted i_m [m/m]
measured i_m [m/m]
(c)

Figure 19

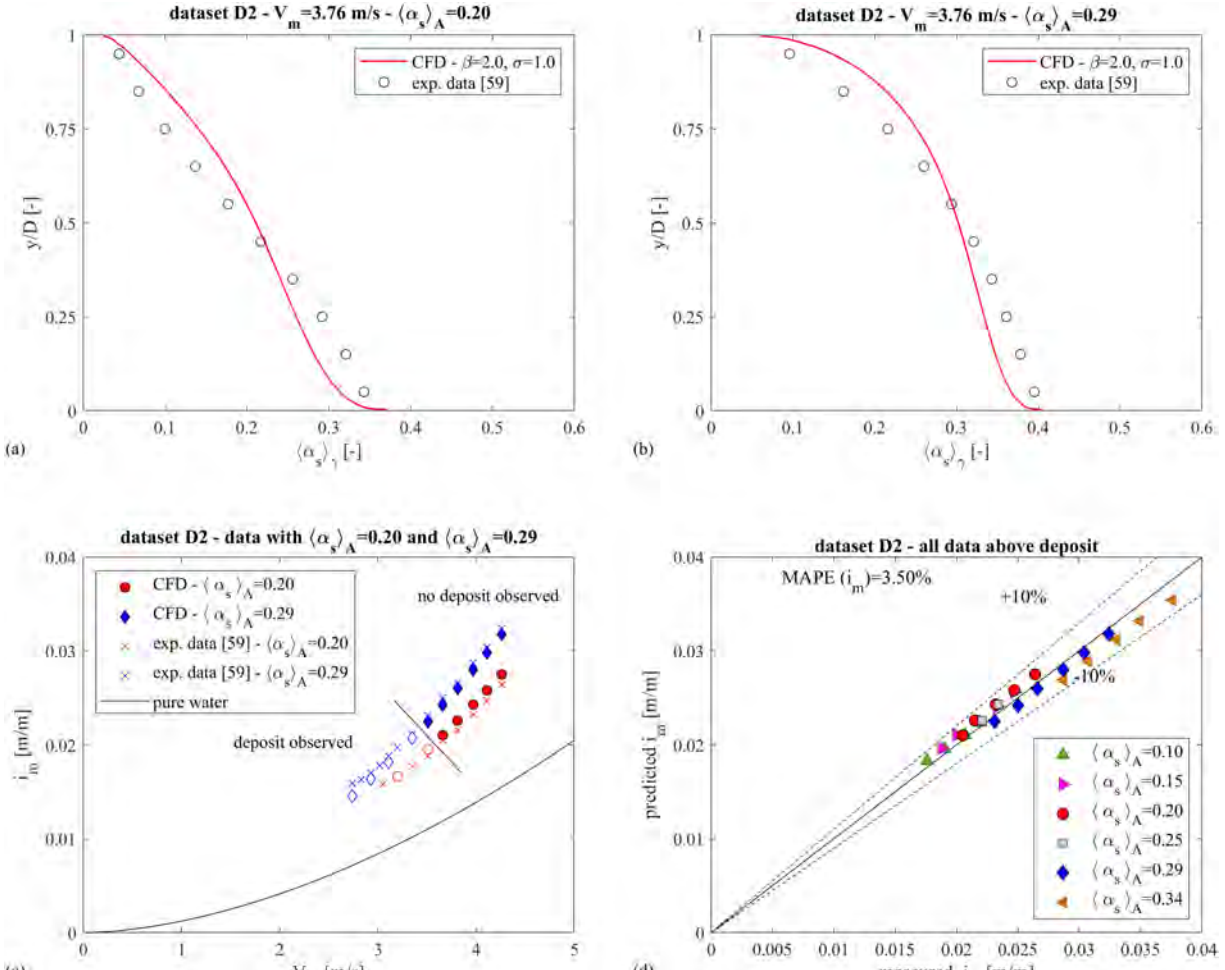
dataset D2 - V_m=3.76 m/s - $\langle\alpha_s\rangle_A$=0.20
CFD - β=2.0, σ=1.0
exp. data [59]
y/D [-]
$\langle\alpha_s\rangle_\gamma$ [-]
(a)
dataset D2 - V_m=3.76 m/s - $\langle\alpha_s\rangle_A$=0.29
CFD - β=2.0, σ=1.0
exp. data [59]
y/D [-]
$\langle\alpha_s\rangle_\gamma$ [-]
(b)
dataset D2 - data with $\langle\alpha_s\rangle_A$=0.20 and $\langle\alpha_s\rangle_A$=0.29
CFD - $\langle\alpha_s\rangle_A$=0.20
CFD - $\langle\alpha_s\rangle_A$=0.29
exp. data [59] - $\langle\alpha_s\rangle_A$=0.20
exp. data [59] - $\langle\alpha_s\rangle_A$=0.29
pure water
no deposit observed
deposit observed
i_m [m/m]
V_m [m/s]
(c)
dataset D2 - all data above deposit
MAPE (i_m)=3.50%
+10%
-10%
$\langle\alpha_s\rangle_A$=0.10
$\langle\alpha_s\rangle_A$=0.15
$\langle\alpha_s\rangle_A$=0.20
$\langle\alpha_s\rangle_A$=0.25
$\langle\alpha_s\rangle_A$=0.29
$\langle\alpha_s\rangle_A$=0.34
predicted i_m [m/m]
measured i_m [m/m]
(d)

Figure 20

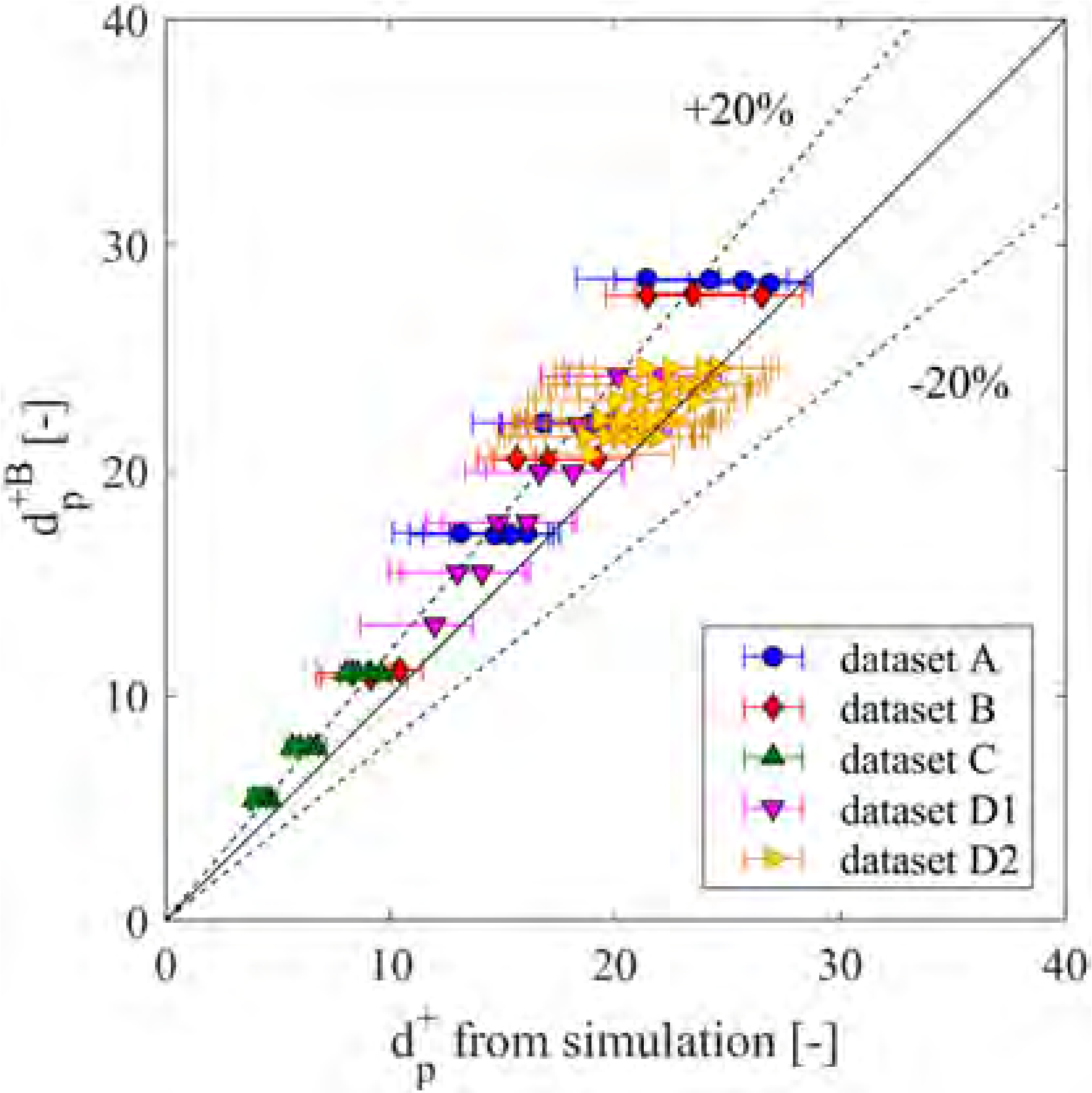
40
30
20
10
0
0
10
20
30
40
+20%
-20%
dataset A
dataset B
dataset C
dataset D1
dataset D2
d_p^{+B} [-]
d_p^+ from simulation [-]

Figure 21

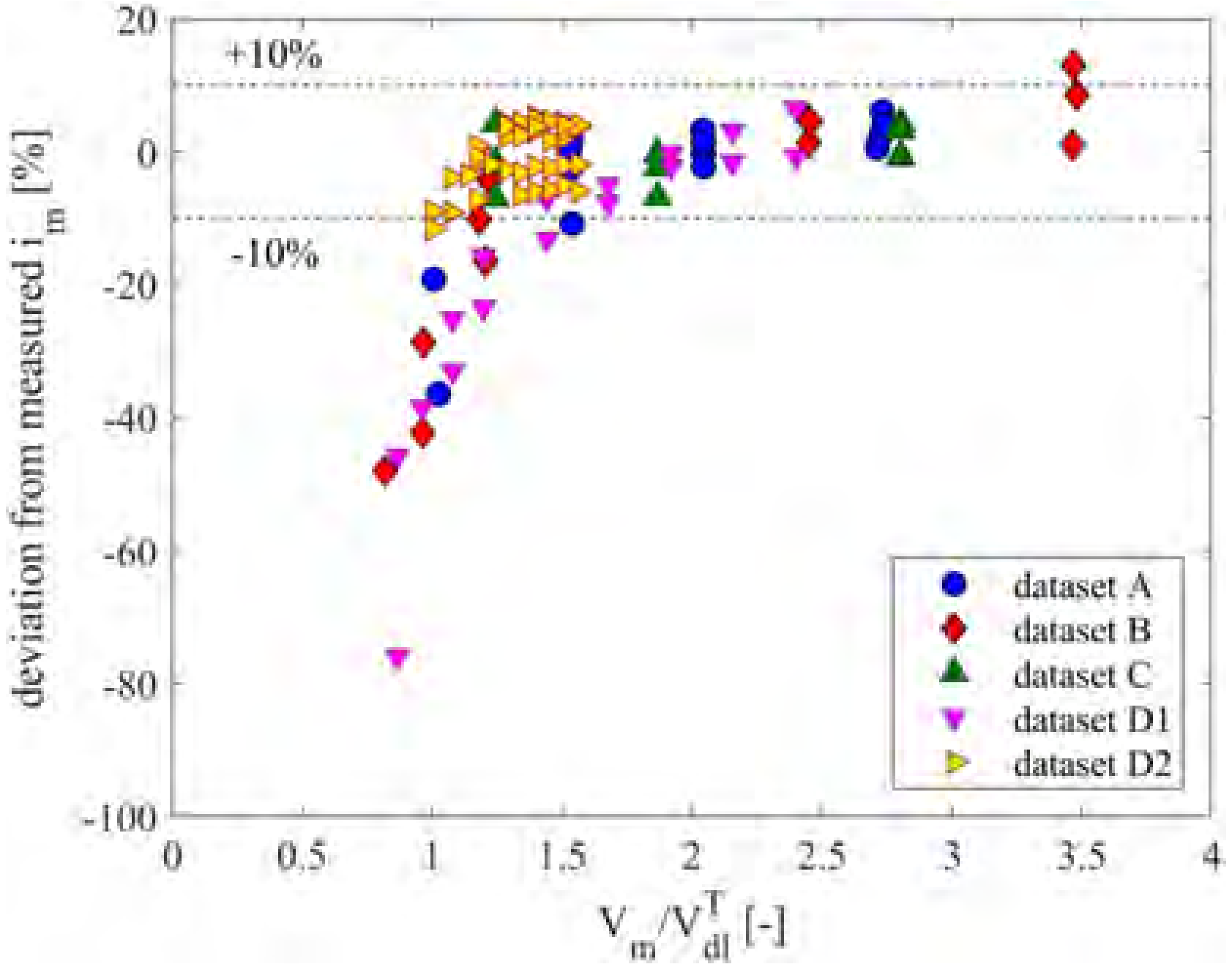
20
0
-20
-40
-60
-80
-100
+10%
-10%
deviation from measured i_m [%]
0
0.5
1
1.5
2
2.5
3
3.5
4
V_m/V_dl^T [-]
dataset A
dataset B
dataset C
dataset D1
dataset D2

Figure 22